Deformable Multi-Modality Image Registration Based on Finite Element Modeling and Moving Least Squares

DEFORMABLE MULTI-MODALITY IMAGE REGISTRATION BASED ON FINITE ELEMENT MODELING AND MOVING LEAST SQUARES

BY

NAVID SAMAVATI, B.Sc.

A THESIS

SUBMITTED TO THE DEPARTMENT OF ELECTRICAL & COMPUTER ENGINEERING

AND THE SCHOOL OF GRADUATE STUDIES

OF MCMASTER UNIVERSITY

IN PARTIAL FULFILMENT OF THE REQUIREMENTS

FOR THE DEGREE OF

MASTER OF APPLIED SCIENCE

© Copyright by Navid Samavati, December 2009

All Rights Reserved

Master of Applied Science (2009) McMaster University

(Electrical & Computer Engineering) Hamilton, Ontario, Canada

TITLE:	Deformable Multi-Modality Image Registration Based on Finite Element Modeling and Moving Least Squares
AUTHOR:	Navid Samavati B.Sc., (Electrical Engineering) University of Tehran, Tehran, Iran
SUPERVISOR:	Dr. Shahram Shirani Dr. Shahin Sirouspour
NUMBER OF PAGES:	xii, 84

To my beloved family and in memory of my young brothers and sisters in IRAN

who lost their lives demanding freedom for their country

Abstract

During the past two decades, there has been an increasing demand for medical image registration. Deformable image registration has a great importance, because the majority of the registration applications deal with the conditions in which the rigid assumption would not create accurate results. Soft tissue organs (e.g. liver, kidney, and prostate) can change in shape during an intervention. Therefore, a sophisticated registration essentially needs to take into account the geometrical deformations.

In this thesis, we study the problem of deformable liver image registration between Magnetic Resonance (MR) and Ultrasound (US) images of the liver. In our approach, a tracking system is proposed to acquire and rigidly register a 2D US image (I_{US}) with the previously taken MR volume. According to the information obtained from the tracking system, a 2D MR image (I_{MR}) is reconstructed as the match of I_{US}. Mutual information is chosen as the similarity measure between the two modalities in our rigid registration problem. A search optimization problem on the registration parameters is then performed, to provide us with a fine tuned reconstructed I_{MR}.

Our proposed strategy begins with visually identifying corresponding anatomical landmarks on I_{US} and I_{MR}. These landmarks are the inputs of the two proposed methods of deformation in this thesis. The first method, Finite Element Modeling (FEM) approach, produces the deformed images based on the linear elasticity and

the static analysis assumptions. This method uses the positions of landmarks to solve a linear system of equations, in order to generate the final deformations of the MR images. The second method of deformation is the Moving Least Squares (MLS). To the best of our knowledge, MLS has never been used in medical image registration. This technique analytically solves a number of least squares problems to find the local rigid transformations. Applying these local rigid transformations on the MR volume creates the deformations throughout the MR images.

In our experiments, Root Mean Square Target Registration Error (RMS TRE) is used as the quantitative measure for the evaluation of performance. FEM-based method produces the best result with an RMS TRE of $7.2mm$, while MLS-based method creates an RMS TRE of $8.9mm$. According to the literature, an accuracy of $7.2mm$ is acceptable for most intra-operative abdominal procedures, particularly those involving the liver. The drawback of FEM-based method is its higher computational complexity. Our implementation of the MLS-based method could be executed at least 20 times faster than that of the FEM-based method. Therefore, in applications, where the accuracy is critical, FEM-based method should be used. The MLS-based method is more suitable of the applications demanding higher speed or a parallel implementation of the FEM-based method can solve the computation speed problem.

Acknowledgements

I would like to thank my supervisors, Dr. Shahram Shirani and Dr. Shahin Sirouspour for their great support and encouragement throughout my masters at McMaster University. Without their invaluable suggestions and constructive comments this project would never be accomplished. I also would like to thank Dr. Michael Noseworthy for his useful comments and tremendous support and help for providing us with the MR images and the equipments for making the phantom.

Many thanks to my family for their endless love, encouragement and support. My special gratitude goes to my sister, Nazanin, for her priceless love, support, encouragement, and her useful suggestions.

I also would like to thank my great friend, Kimia, for her patience, unconditional support and effective technical discussions.

Last but not least, I would like to gratefully appreciate all of my friends' support. They made my life in Hamilton a lot more interesting and fun.

Notation and abbreviations

US : Ultrasound

Magnetic Resonance Imaging : MRI

Radiation Therapy : RT

Computed Tomography : CT

Root Mean Square : RMS

Target Registration Error : TRE

Correlation Ratio : CC

Finite Element Modelin : FEM

Finite Element : FE

Moving Least Squares : MLS

2D US image : I_{US}

2D MR image : I_{MR}

Conjugate Gradient : CG

Singular Value Decomposition : SVD

Field Programmable Gate Array : FPGA

Poly Vinyle Alcohol : PVA

Contents

Abstract **iv**

Acknowledgements **vi**

Notation and abbreviations **vii**

1 Introduction **1**

1.1 Problem Definition 4

1.2 Thesis Contributions and Outline 8

2 Literature Review **10**

2.1 Physical Based Transformations 11

2.2 Function Representation Transformations 15

2.3 Similarity Measures 16

2.4 Overview of the related works 19

3 Proposed Multi-modality Registration Methods **23**

3.1 Initial Rigid Registration 26

3.2 FEM-Based Deformations 32

3.3 FEM Mathematical and Physical Backgrounds 33

3.4 Displacement Vector Generator 39
3.5 Reconstructing 2D MR images 41
3.6 MLS-based Deformations 49
3.7 3D MLS-Based Deformations 54

4 Experimental Results **58**
4.1 Initial and Deformable Registration Results 59
4.2 Computational Speed and Solutions 66

5 Conclusions and Future Work **72**

A Mutual Information **75**

B Phantom Study **77**

List of Figures

1.1 Radio-frequency ablation 2

1.2 Image Guided Surgery 3

3.1 Flow chart of the registration system 24

3.2 Tetrahedral organ mesh 25

3.3 Conversion of the coordinate A into the coordinate B. 26

3.4 Tracking system 28

3.5 Phantom MR and US images 30

3.6 3D interpolation of a pixel intensity of a transformed grid point . . . 32

3.7 Flow chart of FEM-based method 33

3.8 General 3D body for structural analysis 34

3.9 A tetrahedral element 38

3.10 Corresponding control points on I_{US} and I_{MR} 40

3.11 Defining a new node 41

3.12 Displacement of an arbitrary point 47

3.13 MLS Deformation 53

3.14 3D implementation of the MLS algorithm 57

4.1 Mutual information plot 59

4.2 False registration by mutual information 62

4.3 Test MR and US images rigid and nonrigid matches 63
4.4 Reference MR and US images rigid and nonrigid matches-A 64
4.5 Reference MR and US images rigid and nonrigid matches-B 65
4.6 Resolution comparison with FEM 68
4.7 Resolution comparison with MLS 69
A.1 Joint histogram calculation 76
B.2 A T1 weighted 2D MR image of the PVA phantom 78

Chapter 1

Introduction

Image registration is the process of finding the mapping for every pair of points in two or more different images. Images can be taken in various times, with different sensors and from multiple viewpoints. During the past three decades many researchers have focused on this field of study. They have introduced various applications, such as, environmental monitoring, change detection, image mosaicing, weather forecasting, creating super-resolution images, treatment verification in medicine (comparison of the patients data with anatomical atlases), cartography applications (map updating), and computer vision development (target localization, automatic quality control) [35]. In this thesis, we will focus on medical applications of image registration.

Almost one-quarter of all deaths are caused by cancer in the developed countries [2]. Surgery and Radiation Therapy (RT) are the two most popular cancer therapy treatments, while biopsy is of a great importance in diagnosis of cancer tissues. The principle goal in the surgery is to resect cancer cells without any damage to healthy Organs At Risk (OAR). Similarly, in RT, the goal is to deliver the prescribed dose to the target, while minimizing the damage to the neighboring tissues. In the

majority of the biopsy procedures, a needle-shape tool must be inserted into the suspected area of the body to extract cell samples. Hence, there should be an estimate of the current location of the target because of deformations and movements caused by intervention (Figure 1.1).

Figure 1.1: Radio-frequency ablation of a liver mass guided by ultrasound imaging in the CT suite. (picture from [33])

Planning surgery needs information provided by Magnetic Resonance Imaging (MRI) or Computed Tomography (CT) scan. However, these imaging modalities are rarely used intra-operatively. The only modality which has been widely used during the surgery is the Ultrasound (US). Patient's movements during the acquisition, breathing, and heart beat are the main reasons for intra-operative images to be spatially different from pre-operative images. To optimize the so-called image-guided surgery, surgeons should be able to access as much information as possible from patient's anatomy and structure during the operation (Figure 1.2). An optimal image-guided surgery is clinically determined by the amount of bleeding during the

operation. Therefore, the idea of combining pre- and intra-operative modalities is developed. This integration, must be able to introduce geometric differences while keeping modality-specific information content [18].

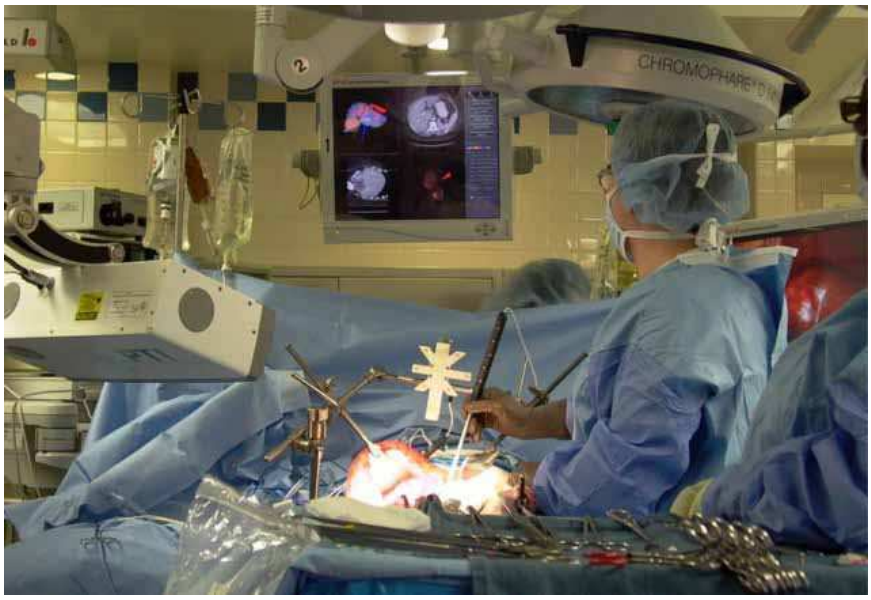

Figure 1.2: Image Guided Surgery. *Courtesy of Vanderbilt University*

From a different clinical point of view, image registration has a great role not only in treatments but also in diagnosis. A challenging problem in abdominal soft tissue organs such as liver and kidney, is the diagnosis of an intermediate lesion. MRI and CT can usually identify the lesion. However, further clinical investigation on the lesion often involves the use of US to determine whether the lesion is benign or malignant. Throughout this procedure, motion or deformation of the organ can lead to a wrong localization of lesion between the two modalities. This can result in a false diagnosis. It is difficult to correlate US images to MR or CT images due to many reasons. Some of the US limitations include: limited field of view, speckle and convolutional noise, and operator-based image acquisition [33]. The main focus of

this thesis is on the deformable and the rigid registration of MRI and US of the liver. Liver is one of the largest organs in our body, and it plays many important and vital roles. However, our proposed techniques can be applied to other soft tissue organs such as kidney, prostate, and breast. This is due to the fact that our assumptions about liver are sufficiently general to be extended to other deformable organs.

There are many ways to combine pre-operatively taken set of images with the online data during the operation. To solve this problem, one must consider what types of transformation can map pre- and intra-operative images. In general, transformations can be divided into three groups; rigid, affine, and nonrigid transformations. In rigid transformations only translational and rotational parameters exist. Affine transformations have two more components; scaling and shearing. Rigid and affine transformations can be represented using homogeneous matrices; 4×4 matrices for 3D to 3D mappings. In the literature, affine transformations are sometimes referred as a subcategory of nonrigid transformations. Nonrigid transformations map straight lines to curves, and therefore, they can cause deformation. This class of transformations is also known as deformable transformations.

1.1 Problem Definition

In this thesis, we mainly concentrate on deformable image registration for liver application. For our problem, we are equipped with pre-operative MR images, while US images are acquired intra-operatively.

The purpose of deformable image registration is to find the relation (transformation) between volume elements (voxels) of different image modalities in the entire image data sets. There are various types of techniques to model the deformations.

Generally, deformation models are divided into two main categories;

- *parametric*: A set of parameters, which represent *a priori* knowledge of the shape structure, is used to model the deformation. There are many parametric transformations that can be employed for deformable registration, for instance, B-Splines, radial basis functions, or the newly developed technique of the Moving Least Squares (MLS) by Schaefer et al. [28]. MLS is chosen as the parametric method of deformation for this thesis. We will elaborate more on MLS-based technique in Chapter 3.

- *non-parametric*: Based on physical properties, the deformation can be determined by solving Partial Differential Equations (PDEs). For the purpose of this thesis, we have selected the static linear elastic modeling and Finite Element Method (FEM) to solve the underlying PDE equations. In fact, we use a Matlab implementation of the Conjugate Gradient (CG) algorithm to solve a linear system of equations arising from Finite Element (FE) models of deformation (as described by Mafi et al. [24]). FEM-based image registration method will be introduced in more detail in Chapter 3.

A comprehensive overview of deformation techniques will be discussed in Chapter 2.

In our research, it is desired to solve two registration problems. The first one is, to find the initial rigid registration between the US image (I_{US}) and the MR volume (V_{MR}). This step involves finding six parameters; three translational parameters and three rotational parameters. The next step, where the main contributions of this thesis lie in, is to find the deformation to be applied on the MR image (I_{MR}) to best match with the I_{US}.

Rigid registration arises in many registration problems. In our work, we add the "initial" term to emphasize the fact that rigid registration is distinct from deformable registration in our framework. The registration problem between I_{US} and V_{MR} can be expressed as an optimization problem. The objective function of the optimization problem is the "*similarity measure*". There has been a tremendous amount of research in this field and various similarity measure functions and optimization methods are available to solve this problem for various purposes. Providing the optimization algorithm of choice with a proper initial value plays a great role in finding a global optimum. Otherwise, the algorithm can easily get trapped in a close by local minimum. A brief overview of the similarity measures is given in Chapter 2.

A common method to find the initial values for the six parameters in our rigid registration problem is to use a tracking system. We have chosen a six Degree of Freedom (DoF) PHANTOM 1.5 Premium Haptic Interface, designed and manufactured by Sensable Technologies, robotic arm. The US probe is connected to the *end effector* of this device, which is the end arm of robotic arm. By this attachment, the coordinate system of the US probe can be represented in the coordinate system of the arm. To obtain the initial values of the six parameters, the relationship between the coordinate system of the probe and the MR volume should be provided. This is a common challenge in many tracking systems, and a well-practiced solution is to employ transformation matrix (we refer to it as "probe-to-MR""), which converts the coordinate system of the US probe to that of the MR volume. In this work, a new method for finding probe-to-MR matrix has been proposed. Chapter 3 includes more details of this method.

Obtaining a 2D image out of a 3D data set is a significant contribution of this

project. In MLS-based approach, finding a 2D view is converted into re-mapping a regular grid, and interpolation of the grid points in a volume. In FEM-based algorithm a more sophisticated approach is introduced in which the deformation is applied simultaneously with forming the image. In Chapter 3 a detailed explanation of the proposed methods is provided.

In FEM-based method, deformable registration is implemented by first building a 3D tetrahedral mesh from the 3D MR volume, then deforming this physical model, and lastly projecting back the deformations to the final 2D image. The latter step is jointly performed with the re-slicing or re-formatting the 2D image out of the 3D MR volume. A new methodology to find the deformation parameters for the 3D mesh has been proposed. Basically, to parameterize the FEM-based method as the deformable transformation model, we need to find the answer to how a 3D mesh can be deformed. From the literature, it is known that a 3D tetrahedral mesh consists of several nodes that make tetrahedral elements. By knowing the displacement of a node and having at least three constrained nodes in the entire mesh, the displacement of every point inside the elements can be determined by means of shape functions, which are just simple interpolants. Consequently, to deform the mesh, some nodes must be selected and displaced in three dimensions. Obviously, the most challenging part of this scenario is finding the number and the indices of the selected nodes to perform the mesh deformation. In the field of optimization, this problem falls under the category of integer programming, which is known to be extremely difficult to solve. In this project, we address the challenge in a new manner to make it simpler.

A visual identification is performed on the I_{MR} and I_{US} to obtain two sets of control points. Each pair of points represents the similar anatomy structure on the

two modalities. The positions of the pairs are used in both methods of deformations in this thesis. In FEM-based method, the control points specify the node numbers and the displacements. MLS-based method uses the control points to form local least squares problems. The solutions of the least squares provide the local rigid transformations. Applying the local rigid transformations to the entire MR volume creates deformed MR images.

1.2 Thesis Contributions and Outline

Physical modeling based on FEM can provide accurate results for image deformation, but its application in the field of deformable image registration is limited due to the difficulties in determining precise boundary conditions of the 3D mesh. In this work, we propose a simplified version of FEM-based method to gain a better and more realistic deformed images without any *a priori* knowledge on the boundary conditions.

We can summarize our main contributions in this thesis as:

- Application of the PHANTOM robotic arm as the US probe tracking system and solving a modified optimization problem to find the probe-to-MR coordinate matrix transformation in the initial rigid registration step.
- A novel FEM-based deformation method to bypass the integer programming problem of the mesh deformation.
- 2D and 3D implementation of MLS-based technique, and application of this method in deformable registration.
- Design and implementation of re-slicing an arbitrary plane inside a 3D data volume.

The rest of this thesis is organized as follows. In Chapter 2, we briefly review and compare the previous works and techniques on mono- and multi-modality deformable image registration. Initial rigid registration, tracking system, the proposed modified optimization scheme to find the probe-to-world coordinate matrix transformation and implementation of re-slicing an arbitrary plane inside a 3D data volume are discussed in Chapter 3. A detailed study on MLS algorithm and FEM-based deformation is also discussed in this chapter. Chapter 4 is dedicated to our experimental results. The thesis is concluded in Chapter 5 with possible future extensions of the present work.

Chapter 2

Literature Review

Image registration is one the most fundamental applications of image processing in the field of medical imaging. In this process, the goal is to find the best alignment between a fixed (source) and a moving (target) image. Technically, a set of geometric transformation parameters, which maximizes a similarity measure cost function, is found to provide us with the best alignment of the fixed and moving image. Consequently, geometric transformation model and similarity measure, the two most important components of the process, should be determined carefully to resolve a registration problem. Depending on the mono- or the multi-modality nature of the images, which will be registered, and the degree of freedom of the geometric transformation, we have to take into account variety of options for these two components. In the following paragraphs, we briefly review and discuss different methods for each components, and finally conclude our proposed combinations for our deformable liver image registration problem.

Rigid-body transformations refer to transformations that preserve the geometrical distance between all points in the image. Translation and rotation are the only

two components in the rigid-body transformation. Affine transformations allow for global change of scale and shear, as well as translation and rotation. These two transformations can be simply represented by homogenous 4×4 matrices to map from 3D to 3D spaces. Non-rigid transformations map a straight line to a curved line. Generally, they are divided into two categories; physical based (also known as non-parametric transformations) models and function representations (also known as parametric transformations). Physical modeling of non-rigid transformations is derived from the continuum mechanics theory, and they can be grouped into two subcategories; elasticity and fluid flow. Function representations are originated from interpolation and approximation theory. Basis function expansions are used to model the deformation. Radial basis functions, B-Splines and Thin-Plate Splines (TPS) are good examples of such functions which are reviewed in this chapter.

2.1 Physical Based Transformations

The linear elasticity theory is explained by concepts of stress and strain. At any location, stress can be defined as the contact force per unit area acting on orthogonal planes that intersect the location. Stress is analyzed by Cauchy stress tensor. This tensor is second rank and denoted by σ_{ij}, the subscripts i and j can be changed with one of the three Cartesian directions. The components of stress are normal to the plane, σ_{ii}, or lie within it , σ_{ij} for $i \neq j$. Since this tensor has nine entries, it can be represented by a 3×3 matrix. Strain is a measure of the amount of deformation. The way it is analyzed mathematically is similar to stress. It is denoted by a second rank tensor, ϵ_{ij}, with normal, ϵ_{ii}, and shear, ϵ_{ij} for $i \neq j$, components.

When a body is under an external force, internal forces are generated within the

body which cause it to deform. The internal forces consist of body and surface forces. Body forces are distributed throughout the volume and they can be specified as force per unit volume. In an equilibrium state, body forces, f, balance with the surface stresses, σ_{ij}, within a linear elastic material. Therefore, the integral of the surface stress forces and the body forces must be equal to zero. By assuming linear stress components across an infinitesimal element, the following set of equilibrium equations can be determined [6]:

$$\frac{\partial \sigma_{xx}}{\partial x} + \frac{\partial \sigma_{xy}}{\partial y} + \frac{\partial \sigma_{zx}}{\partial z} + f_x = 0, \quad (x, y, z) \tag{2.1}$$

where (x, y, z) shows that the other two equations can be provided through cyclic permutation of x, y, and z. Normal and shear infinitesimal strain is expressed in terms of the spatial derivative of displacement as follows:

$$\epsilon_{xx} = \frac{\partial u}{\partial x}, \tag{2.2}$$

$$\epsilon_{xy} = \frac{1}{2}\left[\frac{\partial u}{\partial y} + \frac{\partial v}{\partial x}\right], \quad (x, y, z; u, v, w) \tag{2.3}$$

where (u, v, w) are the displacements along the directions of (x, y, z), respectively. By applying Gauss's divergence theory, it can be shown that the stress tensor σ_{ij} is symmetric. Hence, the number of stress components is reduced to six (σ_{xx}, σ_{yy}, σ_{zz}, σ_{xy}, σ_{yz}, σ_{zx}). The relationship between stress and strain is expressed in the generalized Hooke's law, $\sigma_{ij} = C_{ijkm}\epsilon_{km}$. In this formula, C_{ijkm} is a fourth rank tensor referred to as the stiffness tensor. In a homogenous isotropic material, it is feasible to reduce the number of independent constants in C_{ijkm} to just two (called Lam constants). This reduction is achievable because of the infinite number of "planes

of symmetry" and by considering the rotational invariance. In an isotropic material, the stress strain relation is written in the following Piola-Kirchoff form:

$$\sigma_{xx} = \lambda\delta_{ij}\epsilon_{kk} + 2\mu\epsilon_{ij}, \tag{2.4}$$

where λ and μ are the Lam constants, and μ is also referred to as the shear modulus.

By substituting Eq.(2.2) into Eq.(2.4) and then substituting the resulting expression into Eq.(2.1), gives the Navier-Cauchy linear elastic PDE

$$\mu\nabla^2 u(x) + (\mu + \lambda)\nabla(\nabla.u(x)) + f(x) = 0, \tag{2.5}$$

where $u(x)$ is the displacement vector at position x, and $f(x)$ is the force per unit volume.

The Navier-Cauchy PDE is basically an optimization problem in which the external forces and internal stresses are balanced with smoothness constraints. It can be solved using variational, finite difference, FEM-models, basis function expansion, and Fourier transform methods. The usage of linear elastic models for non-rigid registration was first introduced by Broit in [5]. In his thesis, Broit solved the PDE by finite difference method on a rectangular lattice. The first and the second derivatives are approximated using discrete derivatives, which result to three linear equations, one for each direction. The value of the displacement, u, for each lattice point is calculated using the Jacobi method based on the initial and the previously computed displacements. Inter-subject registration of cortical grey matter is performed using an elastic model in [10]. Their model is based on a balance between internal and external forces that leads to a PDE, which is ultimately solved using successive over-relaxation.

In registration problems with large deformations, fluid flow transformations are typically used. These transformations are based on the non-linear relationship between the stress and the strain. More specifically, a hysteresis in stress-strain curve and stress relaxation can be observed in a viscoelastic material. Unlike a linear elastic model, which is represented by springs, viscoelastic model is presented using springs and dashpots which are connected in series in a Maxwell material and in parallel and series in a Kelvin material. It is worth noting that in a viscoelastic model, stress and strain are functions of time. Christensen et al. [7] proposed a viscous fluid flow model which was applied after linear elastic registration to recover large deformations.

Based on the principle of intensity conservation between image frames, optical flow has been justified to be employed in tracking small scale motions in time sequences of images. Demons algorithm [31] utilizes optical flow to determine the displacement. Due to the fact that there is no constraint on the displacement in this algorithm, it does not necessarily preserve the topology. To reduce the effect of noise, the displacement field is convolved by a Gaussian function to produce a smoother field. During the run of the algorithm, based on the determined displacement field, the source image is resampled for the next iteration.

To benefit more from the continuum mechanics, further investigation on non-linear materials is done to explain the complex behavior of some materials such as soft tissue organs [16]. In his work, Humphery observed that although soft biological tissues have variety of forms, they are composed of only two fundamental components: cells and an extra-cellular matrix. Therefore, tissues could be modelled as an amalgamation of different components and exhibit anisotropy. Consequently, new models can better explain the multi-axial behavior of muscle, growth, damage, regeneration, and cell

mechanics.

2.2 Function Representation Transformations

Transformations based on basis functions do not deal with any physical modeling, but instead they model deformation using a set of coefficients of the basis functions. These coefficients are adjusted so that the total combination of the basis functions fit the displacement field. It should be noted that generally these functions do not preserve the topology. Radial basis functions are functions of the distance of the interpolation point x and the basis function of another point, which is usually a landmark position (x_i). These functions can be defined as follows:

$$f(x) = \sum_{i=1}^{N} \alpha_i R(\|x - x_i\|), \tag{2.6}$$

where N is the number of the landmark positions, α_is are the weights which are determined by solving a set of linear equations, and R defines a type for the radial basis function.

The application of the Thin-Plate Splines (TPS) in medical image analysis was initially introduced by Bookstein [4] to model the shape deformation. As mentioned in [35], it is the most commonly used radial basis function. The TPS is very useful in multidimensional interpolation problems and in applications where smoothness is important. It is usually applicable to registration problems with manually located sets of homologous features and anatomical landmarks in the images. The spline coefficients can also be determined using the least squares [4]. TPS cannot accurately model local deformations, because it is globally supported function. Furthermore,

large deformations can lead to singularities in the equations, which need to be solved, or the topology might not be preserved in the resulting model. Another disadvantage of the global extent is the high computational complexity when large numbers of landmarks are used [14]. Using a cubic B-Spline Free-Form Deformation (FFD) with a voxel similarity measure is proposed by Rueckert et al. [27]. Their algorithm searches for a set of control points which minimizes a cost function. The cost function includes a TPS bending energy term and a normalized mutual information as a similarity metric. The cost function is minimized using a gradient descent method, and regarding the fact that the FFD grids can be reconstructed hierarchically, the deformations can be determined by multiresolution.

The deformations produced by Bookstein [4] can lead to undesirable local non-uniform shearing and scaling. Alexa et al. [1] introduced the concept of as-rigid-as possible deformation in which the amount of local shearing and scaling is minimized. To create such deformations, Igarashi et al. [17] triangulated the input images and solved a linear system of equations with a size equal to the number of vertices of the triangulation. Schaefer et al. [28] improved the method of [17] in terms of the computational complexity, and the quality of final results using a method called Moving Least Squares (MLS), which is the method of choice in this thesis.

2.3 Similarity Measures

Commonly, similarity measures can be grouped into feature-based and intensity-based methods. In feature-based methods, the two images are pre-processed so that the specific images' features or landmarks can be extracted from the two. Regarding how

much the extracted features of each image are moved with respect to the corresponding features of the other image, the transformation parameters or components are estimated. Intensity-based methods deal with minimizing a cost function which is based on a similarity measure of the reference, and moving images' intensities by determining the transformation variables. In the next paragraphs, a review of the most common similarity measures is presented.

The famous family of correlation-like similarity measure is usually computed for window pairs of the reference and the moving images with the following general form

$$CC = \frac{\sum(I_1(i) - \bar{I_1})(I_2(i) - \bar{I_2})}{\sqrt{\sum(I_1(i) - \bar{I_1})^2}\sqrt{\sum(I_2(i) - \bar{I_2})^2}}, \tag{2.7}$$

where $I_j(i)$ represents the intensity of pixel i in the image j.

Although it can exactly align mutually translated images, it can also be successfully applied to more complex geometric transformations. Recently, there has been a great interest in using Cross-Correlation (CC) in multimodal image registration. In this field, the pixel intensities of the same anatomy are different in the reference and the moving images due to different imaging sensors. With the assumption of existence of a correlation function between the pixel intensities in the two images, CC can still be used efficiently. One of the well-known modified form of CC in this case is called Local Correlation (LC):

$$LC = \sqrt{\frac{1}{N}\sum_{S_j \epsilon M} CC^2(S_j)}, \tag{2.8}$$

where CC^2 is the square cross correlation coefficient for the j-th subregion S_j, and N is the number of subregions contained in M. LC has been successfully implemented

in variety of rigid and deformable registration tasks [32]. There has been numerous modifications on CC in literature to address the specified registration conditions [35]. Flatness of the similarity measure maxima due to the self-similarity of the images is the main drawback of the CC. This flatness can be resolved and sharpened by pre-processing and using a vector or edge correlation. High computational complexity is another limitation of CC which can be easily overcome with hardware implementation.

The application of information theory in image registration is considered in a widely used similarity measure called mutual information. The fundamental concept in the definition of the mutual information lies in the statistically significant relationship between pixel intensities of the input images of the registration. Based on Shannon's definition of entropy [29], mutual information is defined as follows:

$$I(A, B) = H(A) + H(B) - H(A, B). \tag{2.9}$$

Mutual information has been studied by many researcher on various applications. In this thesis, an interesting application of the mutual information is in nonrigid registration of multimodality images. In [11], the mutual information is used to recover an un-deformed T1 MR image from a synthetically deformed and intensity changed T1 MR image. The results of the two dimensional (2D) implementation prove the feasibility of this approach [11]. A rigid registration of Ultrasound and MR cardiac images is performed by applying the mutual information to fine tune the final parameters of the registration in [15]. To the best of our knowledge, using the above formula without any further pre- and post-processing step for mutual information to register US and MR without any proper initial guess of the optimal solution seems to be impractical. There are many works on this topic that report a successful registration.

However, a modified version of the mutual information for their specific applications is used [25].

Haber and Modersitzki [12] reported that their proposed similarity metric, which is based on intensity gradient information, outperforms the mutual information. They justified their claim by comparing the behavior of their metric with the mutual information applied to multimodal MR images. However, no US-MR registration result was reported to evaluate the usefulness of the their gradient based similarity metric in that area. There are many more modified similarity metrics based on gradient information and also based on combinations of mutual information with other methods. Based on our experience, generally, the most successful multimodality similarity measure is mutual information.

2.4 Overview of the related works

In this section, a brief overview of the most important related works to our registration project is presented.

In [20], Lange et al. used the center lines of the liver vessels as features and their non-rigid registration between US and MR is reported to improve the Root Mean Square Target Registration Error (RMS TRE) of the vessels by approximately 3-5 mm. A fast registration method based on the Iterative Closest Point (ICP) approach and the Multi-level B-Spline transformation is performed. Then, the best search result of the specific anatomical feature pairs on the centerlines of the vessels of the intra- and pre-operative images is found. The centerlines of the vessels are extracted from segmented pre-operative MR and CT images, and the intra-operative power doppler US images. They conclude that their proposed registration method is fast enough for

clinical application in liver surgery. They claim that their initial accuracy results are promising and must be further evaluated, especially in the operating room.

Craene et al. applied the finite element deformation model and the mutual information as their metric to obtain a non-rigid registration of the pre-operative and the post-procedural images of tumor Radio-Frequency (RF) ablation in the liver [9]. Simultaneous Perturbation Stochastic Approximation (SPSA) is their method of optimization for the cost function, which contains a mutual information term and a weighted term based on the linear elastic energy, to balance the action of similarity measure. In each step, the gradient of the cost function is determined using the finite difference method, and in the next step different perturbations of the subset of the active vertices, to stochastically estimate the mutual information gradient, are performed. Then, the average mutual information is added to the cost function. Their algorithm is parallelized for symmetric multi-processor architectures.

Blackall et al. [3] report a registration accuracy to within 10 mm between free-hand US and MR images of liver. This accuracy is reached by an optically tracked US probe and the use of models of respiratory motion and deformation. Their motivation was to transfer information from the pre-operative 3D MR or CT images to the intra-operative US images to help the needle insertion procedure in thermal ablation of liver metastasis. To achieve suitable evidence of the corresponding structure, they introduced an intermediate mapping from both sets of images (intra- and pre-operative) to probability images. This pre-processing step results in more consistency in the behavior of their similarity metric (Normalized Cross Correlation (NCC)) and provided their registration with successful results. Nonrigid registration is accomplished by acquiring different MR or CT volumes in various phases of breathing (from inhale

to exhale) in order to compensate the deformation caused by breathing. With this strategy, 2D US scans can be done anytime during a breathing cycle. They also eliminated the effects of the US probe pressure by ignoring the first few centimeters of the US images.

Combining anatomical landmark information as a constraint, and normalized gradient field as the intensity measure improves the mean of point distances above 3 mm in comparison with the rigid and the thin-plate spline registration which are based only on landmarks [21]. TPS registration is the fundamental method of nonrigid registration in [21]. To obtain a better match, the intensity information is also integrated into the optimization problem as a constraint. The objective function consists of a normalized gradient field as a similarity measure and a regularization term, which indicates the level of smoothness of the deformation field. The optimization is solved using a Discretize-Optimize approach. It is also reported that the clinical validation of the deformable registration is challenging, and it depends on the specific application that the registration problem is solved for.

Wein et. al developed an automatic rigid and affine CT-US registration by proposing a robust similarity measure based on simulating US from CT, resulting in average RMS TRE of 8.1 mm [33]. They used a tracking setup to find an initial estimate of the orientation of the selected US frame. The automatic US frame selection criteria is based on the entropy of the US images. This enables the final selected US images to contain fine unique vascularity. A modified Correlation Ratio (CR) similarity measure is also proposed. The most important advantage of this similarity measure called, LC^2, is taking into account the importance of alignment of small vascularity,

which is essential in a correct registration within the liver. Basically, the simulation of an image from a CT image, which has most of the characteristics of an US image, results in such minimum or maximum points on similarity measure function. This simulation is accomplished by considering the relationship between the X-ray attenuation coefficient and the tissue density.

Chapter 3

Proposed Multi-modality Registration Methods

The flow chart of our system of deformable registration between 2D US images and 3D MR volume is displayed in Figure 3.1. We first find a rigid registration between a 2D US image (I_{US}) and a 2D MR image (I_{MR}), which is reconstructed from the 3D MR volume. The probe used in our experiments is attached to a six degree of freedom arm as the tracking system. It acquires I_{US} as the reference image for our registration algorithm. This 2D image contains sufficient amount of features to be matched with the correct I_{MR}. A 2D MR image, $I_{MR}^{initial}$ is reconstructed by means of three translational and three rotational parameters, which are the outputs of the tracking device. All of these parameters are converted from the coordinate system of the probe to the coordinate system of MR volume (we discuss this conversion in more details in Section 3.1). This image is further investigated by a local search on these six parameters' neighborhoods using the mutual information as the similarity measure to produce the accurately matched image, I_{MR}. The process of rigidly matching of I_{US}

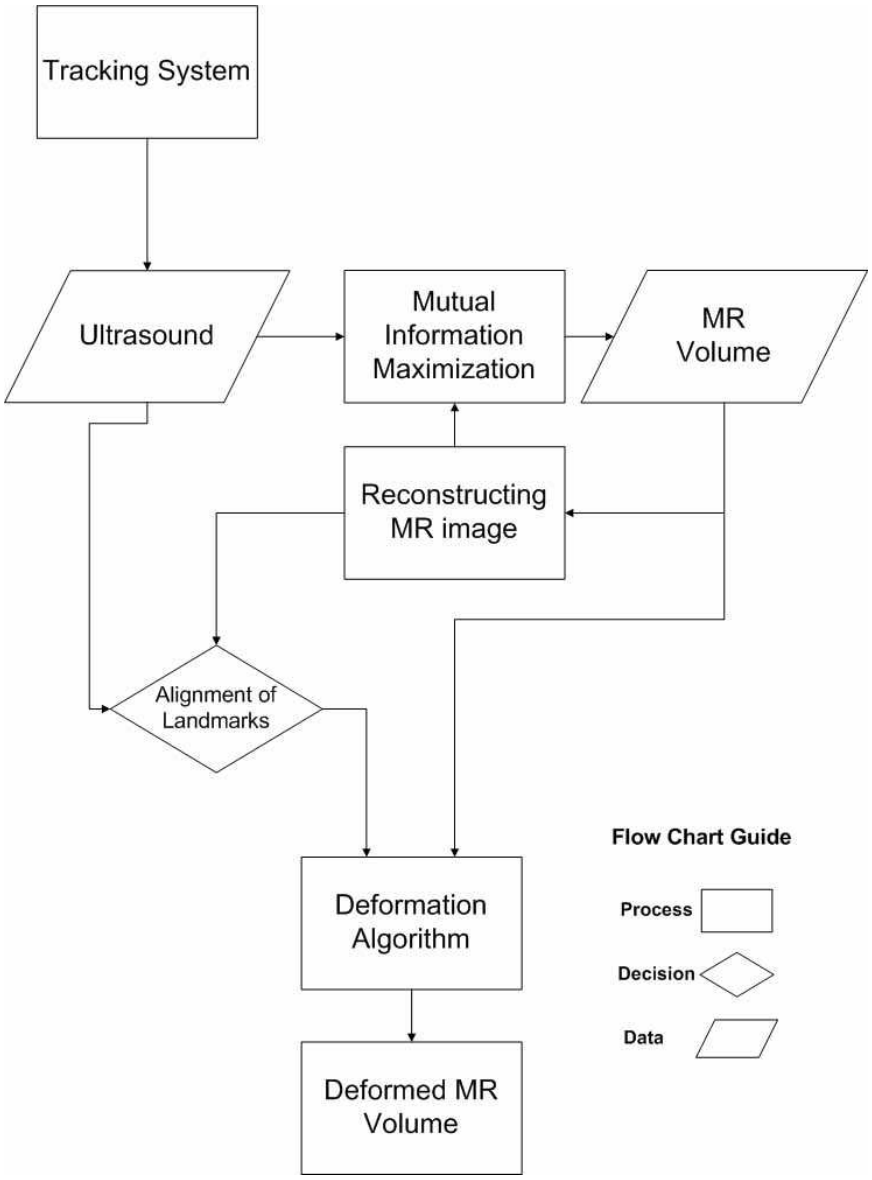

Figure 3.1: Flow chart of the proposed algorithm for deformable registration between 2D US and 3D MR images

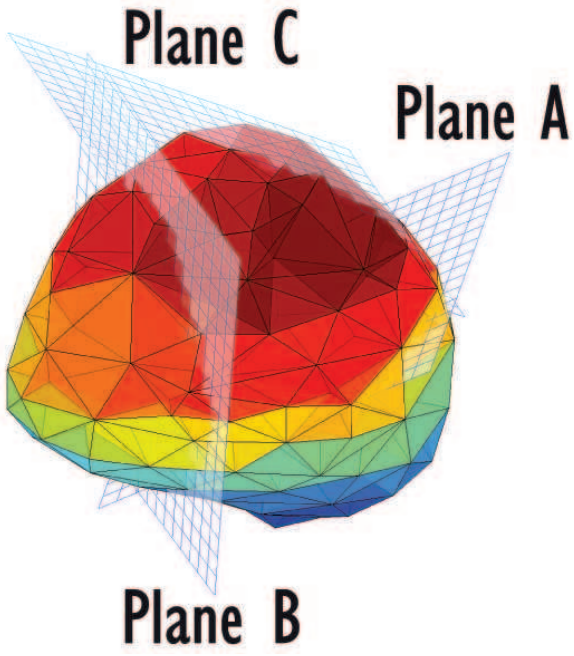

Figure 3.2: Tetrahedral liver mesh. Planes A and B are used as the reference planes for finding the control points. Plane C is used to evaluate the registration accuracy.

and I_{MR} is repeated for another acquired 2D Us image. In Figure 3.2, Plane A and Plane B represent geometrical views of two MR images, which are rigidly matched with their corresponding 2D US images. By selecting some points on these two images' planes as the control points, which act as the inputs of our deformation algorithms, we deform the 3D volume using FEM-based and MLS-based methods to achieve the best possible non-rigid registration. We should note that the reconstructed MR image on Plane C will be used to verify the registration accuracy in Chapter 4. In Section 3.2, we discuss an overview of the FEM-based deformation method, and in Section 3.6 we explain how MLS-method deforms the MR images.

3.1 Initial Rigid Registration

The US probe is attached to a six Degree of Freedom (DoF) robotic arm (Figure 3.4(a)). The output of this tracking system is a matrix which can convert the coordinate system of the tip of the arm, that is referred to as *end-effector*, to the global coordinate system of the arm. This 4×4 matrix has the following form

$$T_A^B = \begin{pmatrix} R_{11} & R_{12} & R_{13} & T_x \\ R_{21} & R_{22} & R_{23} & T_y \\ R_{31} & R_{32} & R_{33} & T_z \\ 0 & 0 & 0 & 1 \end{pmatrix}, \tag{3.1}$$

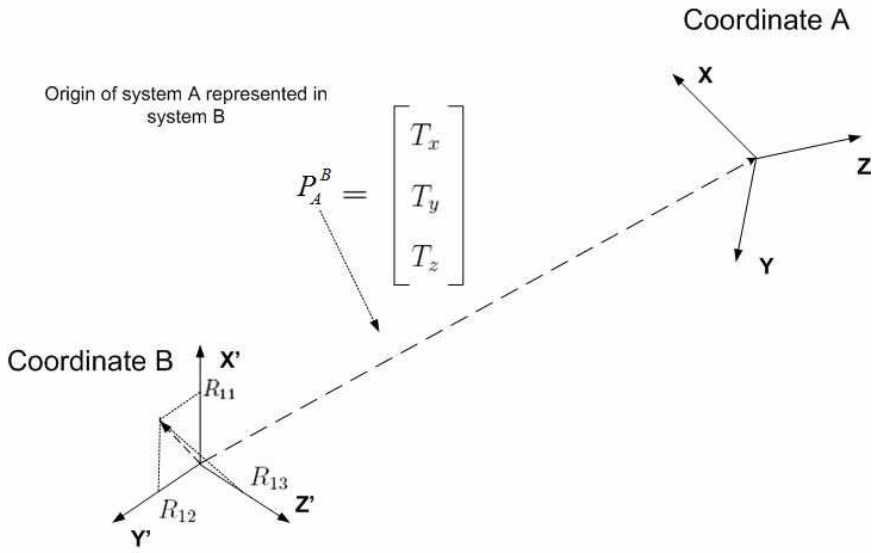

Figure 3.3: Conversion of the coordinate A into the coordinate B.

where R_{ij} represents the projection of the axis i of the coordinate system A into the axis j of the coordinate system B, and T_i shows the translation in i direction, Figure 3.3. Rotation matrix (the 3×3 matrix, R, constructed from the first three

columns and rows of T_A^B) has six constraints on its elements. In summary, we can say $RR^T = I$. Therefore, it can be minimally represented by three parameters. In other words, three parameters are sufficient to describe the orientation of a coordinate system, and in total T_A^B contains only six independent parameters. α, β, and γ are the angle of rotation with respect to axis X, Y, and Z.

In our experiments, we used the tracking system on a phantom. The phantom should be deformable and multi-modality. We made a PVA cryogel phantom (for further information about the phantom refer to appendix B). This phantom can be thought of as a replacement for the patient. Therefore, the following explanation holds for both patient and phantom study. Throughout the following explanation, wherever the patient case is pointed out, the equivalent phantom case is clarified in the parentheses.

In our framework, we essentially need to know the orientation and the translation of the US plane in the coordinate system of the patient's body (phantom), or technically, in the 3D MR data set. The transformation matrix, which converts the coordinate system of the MR data set to the coordinate system of the US probe, is indicated by T_{Probe}^{MR}. This is the most important unknown of our initial rigid registration problem. Accordingly, T_{End}^{Arm} is the transformation matrix that converts the coordinate system of the end-effector of the robotic arm to the coordinate system of the arm (see Figure 3.4(b)). T_{End}^{Arm} is homogenous transformation relating the end-effector frame and the robot base frame. This transformation is a function of joint measurements and is calculated using the device forward kinematics [30]. Therefore, we can write

$$T_{Arm}^{MR}.T_{End}^{Arm}.T_{Probe}^{End} = T_{Probe}^{MR}, \tag{3.2}$$

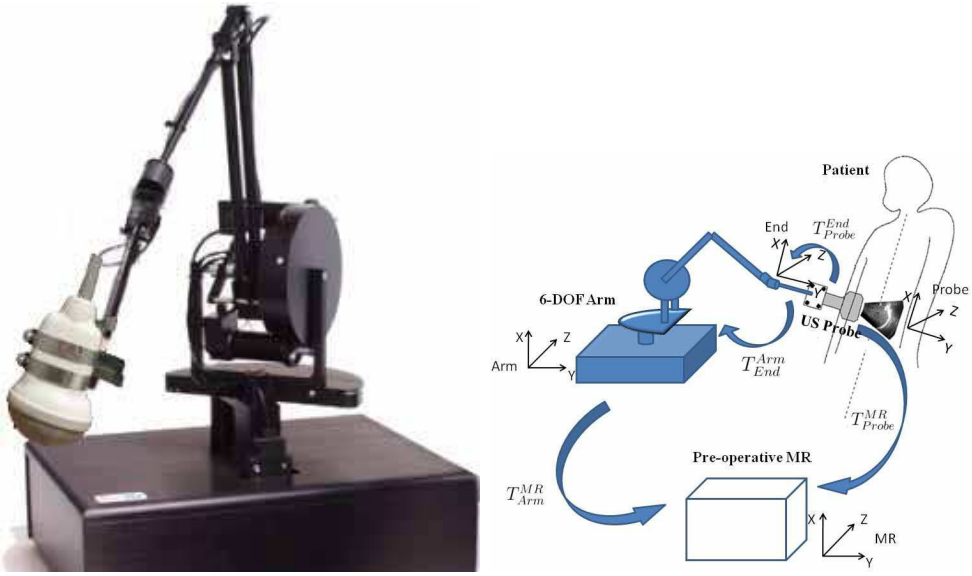

(a) Tracking 6-DoF arm (b) Tracking framework.

Figure 3.4: (a) Tracking arm's end-effector is attached to the US probe. (b) Transformation matrices are also illustrated in order to provide a schematic view of the entire US image acquisition and initial rigid registration.

where all the parameters describing T^{MR}_{Arm} and T^{End}_{Probe} are unknown.

It should be noted that the strategy to find the unknown parameters is to form an optimization problem by introducing a cost function based on the known parameters. We assume that we know the position (or the translation) parameters of the US probe in the coordinate system of the MR data set for some points. These points can be some skin markers or equivalently some features on the MR data set that the US probe can be manually placed to the corresponding surface positions on the patient's body (the edges of phantom's container). The process starts with selecting a point on the tip of the probe (P_{Probe}) that its position is known relative to the coordinate system of the end-effector of the arm. Then, by touching the surface features of the patient's body (the edges of phantom's container) with the probe (exactly on P_{Probe}),

we can obtain the following equation:

$$T_{Arm}^{MR}.T_{End}^{Arm}.T_{Probe}^{End}.P_{Probe} = P_i, \tag{3.3}$$

where P_{Probe} is the constant point selected on the probe represented in the coordinate system of the probe, and P_i is the i^{th} point (feature) on the patient's body (the edges of phantom's container) represented in the coordinate system of the MR data set. If we continue forming this equation for every feature on the patient's body, then we will be able to derive the following cost function:

$$C = \sum_{i=1}^{N} ||T_{Arm}^{MR}.T_{End}^{Arm}.T_{Probe}^{End}.P_{Probe} - P_i||^2, \tag{3.4}$$

where N is the number of observation (feature) points and $||.||$ denotes norm 2. The goal is to minimize this cost function by finding the optimal unknown parameters in T_{Arm}^{MR} and T_{Probe}^{End}. This optimization problem is an unconstrained non-linear problem with the total number of twelve unknowns, and can be solved using one of the standard non-linear optimization packages. Obviously, each point (feature) generates three independent equations. Therefore, to produce a more accurate solution, we include more than $\frac{12}{3} = 4$ points to have an over-determined system of equations. Solving an over-determined system of equations will decrease the effect of noisy measurement's precision. For our application, we decided to have eight points (features). After finding the unknown parameters, we can multiply T_{Arm}^{MR}, T_{End}^{Arm}, and T_{Probe}^{End} together to obtain T_{Probe}^{MR}. This means that when we acquire an US image then the position and the orientation of that image is available in the coordinate system of the 3D MR data set. Figure 3.5 displays the acquired 2D US image and the 2D reconstructed

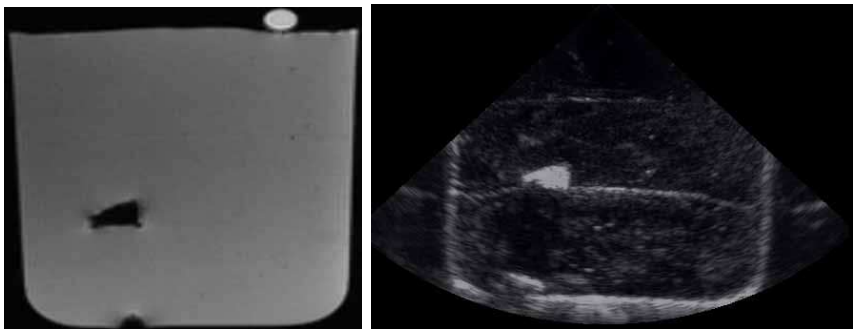

(a) 2D reconstructed MR image

(b) Acquired 2D US image

Figure 3.5: The acquired 2D US image and the 2D reconstructed MR image based on the six output parameters of the tracking system. The US image is taken from the top layer of the PVA gel. The two images are rigidly match.

MR image based on the output of the tracking system in our phantom study. These six parameters are the inputs to our intensity based algorithm to further optimize and tune the final reconstructed I_{MR}. In the rest of this section, we explain how a 2D MR image is reconstructed from a 3D data set while having the six parameters of the position and the rotation (orientation).

In this thesis, for the rigid registration of the patient data, the tracking system is not used due to the difficulties in accessing to the proper skin markers, that can be seen on MR images and remain fixed relative to the patient position. However, one can overcome this problem by having access to these specialized markers. Therefore, in the absence of the tracking system, our back-up strategy is to use a manual global search of the rigid parameters. Hence, before starting the intensity-based local search for the three rotational and the three translational parameters, the initial values of them can be still available.

To find an arbitrary 2D projection of a 3D data set, an initial 2D grid parallel

to one of the principle planes (e.g. XY, XZ or YZ) is built. We should note that a 2D grid basically consists of three 2D matrices, each containing one of the X, Y, and Z position values of all the grid points. The density or the resolution of this 2D grid depends on the pixel spacing of I_{US} and $I_{MR}^{initial}$. The pixel spacing information of both images are available in the header file coming with the raw images. Our purpose is to find $I_{MR}^{initial}$ which matches with I_{US}. It means that the physical space between two neighboring pixels in $I_{MR}^{initial}$ and I_{US} should be the same. Normally, I_{US} has smaller pixel spacing than MR volume. So, the spacing between the initial 2D grid can be the same as the pixel spacing of I_{US}. The reason is to maintain the highest possible resolution (in terms of underlying anatomical structure). The next step is to transform this grid to the newly found plane. The transformation matrix contains the six parameters of the position and the orientation available from the tracking system. Then, for every new transformed grid point, using a 3D linear interpolation, a pixel intensity is estimated (see Figure 3.6). It must be emphasized that pixel intensities of the 3D MR data set with their fixed and regular positions are being used to interpolate the pixel intensity for each grid point on this specific plane. These intensities are placed as the entries of a 2D matrix, which can be displayed as a new reconstructed 2D MR image.

The final step is to further optimize this reconstructed 2D MR image, $I_{MR}^{initial}$, by changing the six parameters of its plane to achieve the best match between this image and I_{US}. The criteria chosen to measure the similarity between the images is the mutual information. As introduced in Chapter 2, mutual information is reported to be the most suitable similarity metric for multi-modality (MR-US) comparisons. Our strategy to obtain a fine tune of the six parameters is to search within an interval

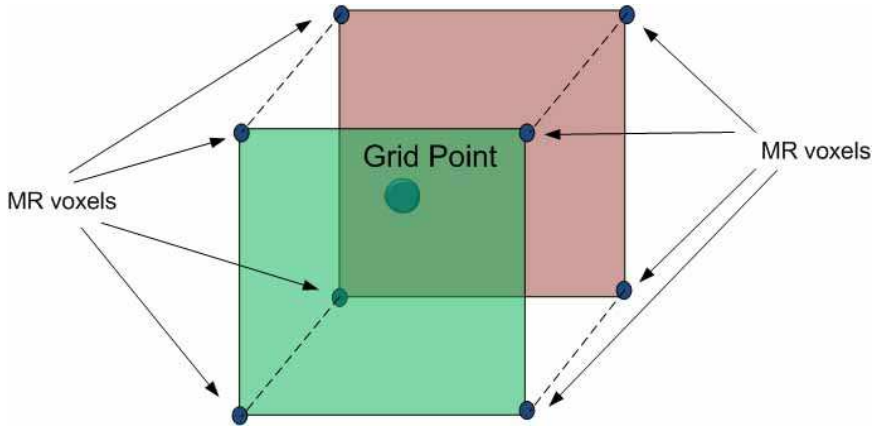

Figure 3.6: 3D interpolation of a pixel intensity of a transformed grid point

around each parameter's initial value, and determine the mutual information for each value. In Appendix A, a more detailed study on how to calculate the mutual information between two images is presented. The best image is the one with the highest amount of mutual information. It is necessary to point out that to compute the mutual information between any two images, they must be in the same size. Therefore, I_{MR} is cropped to the size of I_{US}.

3.2 FEM-Based Deformations

The flow chart displayed in Figure 3.7, illustrates an overview of how our proposed FEM-based algorithm deforms the MR volume. In this flow chart, liver segmentation and building the 3D mesh are pre-processing steps. The main parts of this chart are the reconstructing 2D deformed MR image from the deformed mesh, and the displacement vector generator. Initially, we study the mathematical backgrounds and the physics fundamentals of the FEM to have a better understanding of the deformations generated by this algorithm. Then, we extensively discuss the two main

blocks of the flow chart, reconstruction of the 2D MR image and the displacement vector generator.

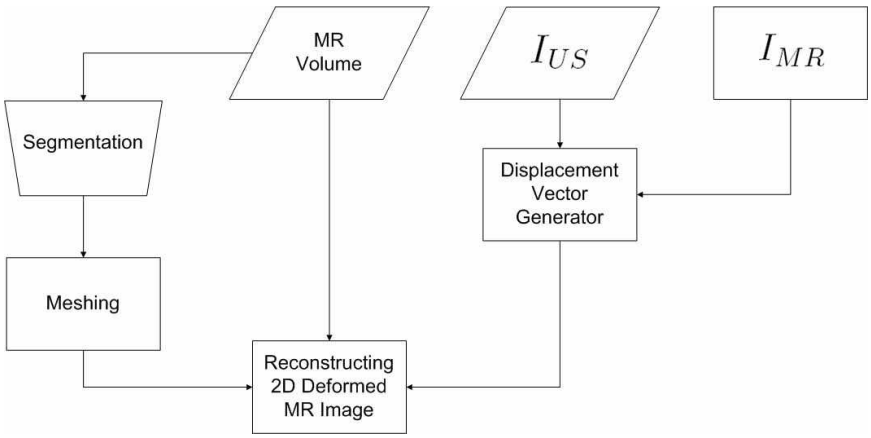

Figure 3.7: Flow chart of the proposed algorithm for deformable registration between 2D US and 3D MR images

3.3 FEM Mathematical and Physical Backgrounds

The main idea in FEM is to spatially discretize the deformation model. In our case, we model the deformation with the linear elasticity assumptions that leads solving partial differential equilibrium equations of the object under the condition of small deformation. Hence, the geometry of the object is partitioned into smaller elements. The shapes of these elements are specified by means of a mesh which covers the desired geometry. The continuous form of the solution is determined by interpolation functions for every point inside each element. These functions are based on the displacement of the nodes specifying the element. To have a better perspective of FEM formulation, we consider a 3D object displayed in Figure 3.8 in equilibrium. Surface S_c is where the body is constrained with prescribed displacement of u_S. It is

also exposed to body forces distributed over the volume denoted by f_b (e.g. gravity force), surface forces f_S distributed on S_u (e.g. pressure) and concentrated loads, R_i [23].

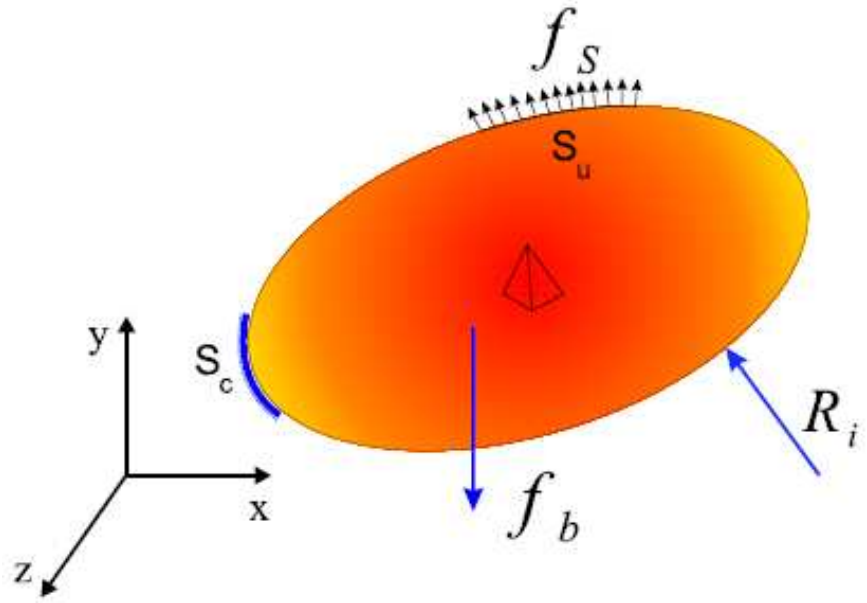

Figure 3.8: General 3D body for structural analysis (Taken from [23])

As discussed in Chapter 2, there is a relationship between strain and displacement, and it can be represented by the following matrix form:

$$\boldsymbol{\epsilon} = L\mathbf{u}, \tag{3.5}$$

where $\mathbf{u}^T = [u \quad v \quad w]$ and L is in the form of

$$L = \begin{pmatrix} \frac{\partial u}{\partial x} & 0 & 0 \\ 0 & \frac{\partial u}{\partial y} & 0 \\ 0 & 0 & \frac{\partial u}{\partial z} \\ 0 & \frac{\partial u}{\partial z} & \frac{\partial u}{\partial y} \\ \frac{\partial u}{\partial z} & 0 & \frac{\partial u}{\partial x} \\ \frac{\partial u}{\partial y} & \frac{\partial u}{\partial x} & 0 \end{pmatrix}, \tag{3.6}$$

The relationship between stress and strain can be obtained using generalized Hooke's law in the following form:

$$\boldsymbol{\sigma} = D\boldsymbol{\epsilon}, \tag{3.7}$$

where D, the stress-strain matrix for linear homogenous and isotropic materials, is related to Poisson's ratio ν and Young's elasticity module E in the form of

$$D = \begin{pmatrix} \lambda + 2\mu & \lambda & \lambda & 0 & 0 & 0 \\ \lambda & \lambda + 2\mu & \lambda & 0 & 0 & 0 \\ \lambda & \lambda & \lambda + 2\mu & 0 & 0 & 0 \\ 0 & 0 & 0 & \mu & 0 & 0 \\ 0 & 0 & 0 & 0 & \mu & 0 \\ 0 & 0 & 0 & 0 & 0 & \mu \end{pmatrix}, \tag{3.8}$$

and Lamé's constants λ and μ are defined as

$$\lambda = \frac{E\nu}{(1+\nu)(1-2\nu)}, \tag{3.9}$$

$$\mu = \frac{E}{2(1+\nu)}. \tag{3.10}$$

The development of the deformation equations are based on the virtual work principle for an object in equilibrium state. This principle states that the total amount of external virtual work is equal to the total amount of internal virtual work for an object in equilibrium. This can be written in the following form [23]

$$\int_V \bar{\boldsymbol{\epsilon}}^T \boldsymbol{\sigma} dV = \int_V \bar{\mathbf{u}}^T f_b dV + \int_S \bar{\mathbf{u}}_S^T f_S dS + \sum_i \bar{\mathbf{u}}_i{}^T R_i, \tag{3.11}$$

where $\bar{\boldsymbol{\epsilon}}$ is the virtual strain corresponding to the virtual displacement $\bar{\mathbf{u}}$. In equilibrium state, the external loads in the right hand side of the Eq. (3.11) is related to the stress, $\boldsymbol{\sigma}$. The internal virtual work is on the left hand side of this equation, whereas the right hand side of this equation contains the virtual work by external forces. To emphasize that the virtual displacements and the corresponding strains are unrelated to the real deformation and strain that the body undergoes given the external loads and restrains of the problem described for Figure 3.8, the overbar notation is used.

Our objective here is to find the virtual displacement $\bar{\mathbf{u}}$. In most cases, there is no analytical solution for Eq. (3.11). Therefore, we need to geometrically descritize the region where the PDEs should be solved. There are many ways to partition the space, but in this thesis we will use a tetrahedral mesh to model the liver. This mesh contains a number of nodes and an elemental matrix in which every row indicates the node numbers required to specify an element. These elements are overlapping only

through the nodes, which are nothing but some points. Figure 3.2 shows a tetrahedral mesh for liver.

For an arbitrary point inside an element, we have

$$\mathbf{u}^e(x, y, z) = N^e(x, y, z)\hat{U}, \tag{3.12}$$

where superscript e indicates element e, $\mathbf{u}$ is the nodal displacement vector of the element, $\hat{U}$ is the general nodal displacement vector[1] of the mesh, and $N^e(x, y, z)$ is the interpolation function for the element e. The details of $N^e(x, y, z)$ will be derived in Section 3.5. Similarly, we can express the elemental strain parameter based on the general nodal displacement vector

$$\boldsymbol{\epsilon}^e(x, y, z) = L\mathbf{u}^e(x, y, z) = LN^e(x, y, z)\hat{U} = B^e(x, y, z)\hat{U}. \tag{3.13}$$

We denote matrix $LN^e(x, y, z)$ as $B^e(x, y, z)$. The element displacements and strains are defined in terms of the general displacement vector $\hat{U}$. At this stage, Eq. (3.11) can be written as

$$\sum_e \int_{V^e} \bar{\boldsymbol{\epsilon}}^{eT} \boldsymbol{\sigma}^e dV^e = \sum_e \int_{V^e} \bar{U}^{eT} f_b^e dV^e + \sum_e \int_S^e \bar{U}_S^{eT} f_S^e dS^e + \sum_i \bar{U}_i^{\,T} R_i, \tag{3.14}$$

where $\bar{U}^e$ is the virtual displacement within each element and $\bar{\boldsymbol{\epsilon}}^e$ is the corresponding

[1]It should be noted that in order to distinguish between the nodal displacement vector and the general nodal displacement vector, we use upper case for the latter. Any other upper case notation indicates a matrix.

strain. Substituting Eqs. (3.12) and (3.13) and (3.7) in Eq. (3.14), we obtain

$$\bar{\hat{U}}^T \left(\sum_e \int_{V^e} B^{eT} L^e B^e dV^e \right) \hat{U} = \bar{\hat{U}}^T \quad \left[\left(\sum_e \int_{V^e} N^{eT} f_b^e dV^e \right) + \left(\sum_e \int_{S^e} N_S^{eT} f_S^e dS^e \right) + \sum_i R_i \right]. \tag{3.15}$$

Removing $\bar{\hat{U}}$ from both sides of the Eq. (3.15) and denoting the global nodal displacement by U instead of $\hat{U}$, the remaining terms can be expressed as

$$KU = f, \tag{3.16}$$

where $U \in \Re^{3n}$ is the vector of nodal displacement, $f \in \Re^{3n}$ is the vector of nodal forces, and $K \in \Re^{3n \times 3n}$ is the global stiffness matrix of the mesh given by

$$K = \sum_e K^e = \sum_e \int_{V^e} B^{eT} L^e B^e dV^e. \tag{3.17}$$

The right hand side of Eq. (3.15) is the external force vector on the exerted nodes [23].

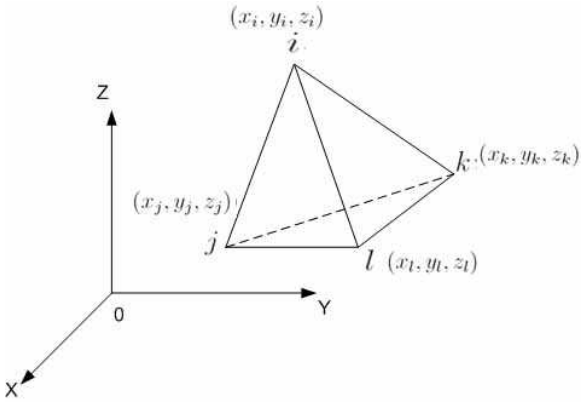

Figure 3.9: A tetrahedral element

3.4 Displacement Vector Generator

Our proposed technique to deform the mesh starts with choosing some control points (P_{US}) on I_{US} as the features and also the corresponding points (P_{MR}) that resemble the same anatomy structure on I_{MR} (see Figure 3.10). These features are mostly on the bifurcation points, the vessel walls, and the center lines of the vessels. The outputs of this step are the displacement vectors of some particular nodes of the 3D mesh. Later in this section, we give an explanation on how to identify these particular nodes. We have two pairs of rigidly matched MR and US images; one on Plane A and another on Plane B (see Figure 3.2). Although I_{MR} and I_{US} are rigidly matched, but there are some deformations between the structures of the two images due to the fact that

$$P^i_{US} \neq P^i_{MR} \quad i = 1..N, \tag{3.18}$$

where N is the number of control points.

Our goal is to find a deformable transformation that deforms I_{MR} so that if one selects the same anatomy structures (producing P^i_{MR}), then $\sum_{i=1}^{N}(|P^i_{US} - P^i_{MR}|)$ will be minimum. Such a transformation is presented in this section using FEM-based linear elastic deformation model. Section 3.6 discusses the transformation obtained by MLS.

In the FEM-based approach, since the mesh and the 3D MR data have the same coordinate system, we are able to find the tetrahedral element inside the organ mesh that contains the first control point, P^1_{MR}. This point is the candidate to be a new node, and therefore the element is broken into four smaller elements as shown in Figure 3.11. After updating the mesh, the algorithm continues this process for every

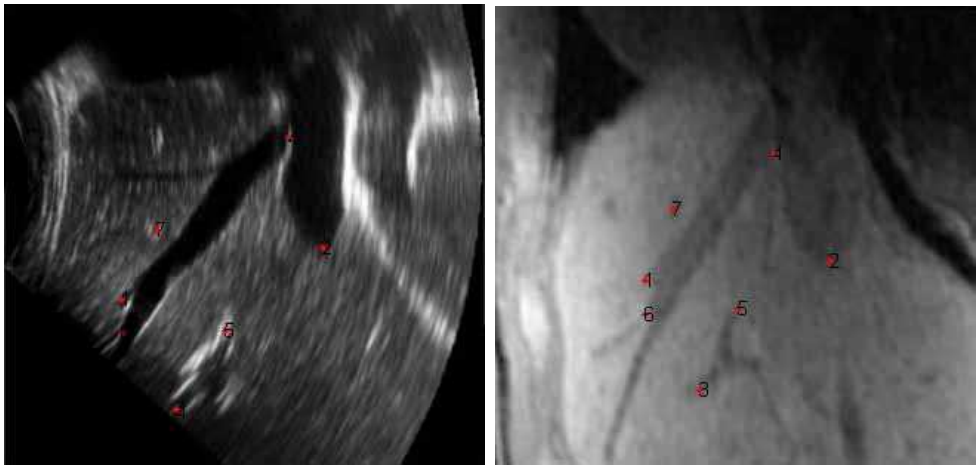

(a) Control points on I_{US} (b) Control points on I_{MR}

Figure 3.10: Corresponding control points on I_{US} and I_{MR}

control point to the last control point. Now, there are N nodes inside the organ mesh with known deformation values ($U_i = P^i_{US} - P^i_{MR}$). In order to apply this type of boundary condition, in Eq. (3.16), all but the diagonal elements of the rows and columns, corresponding to these N nodes, in matrix K are set to zero. The diagonal entries are set to one and force vector f is changed to account for the multiplication of the deleted rows and columns by the known displacements of the N nodes (further details of the process is explained in [24]). Therefore, Eq. (3.16) can be solved to create the deformed mesh. The Conjugate Gradient (CG) method, which benefits from the symmetry and the positive-definiteness of matrix K, is an effective method to solve this system of equations. A highly parallel implementation of the CG on an Field Programmable Gate Array (FPGA) device is introduced by Mafi et al. [24].

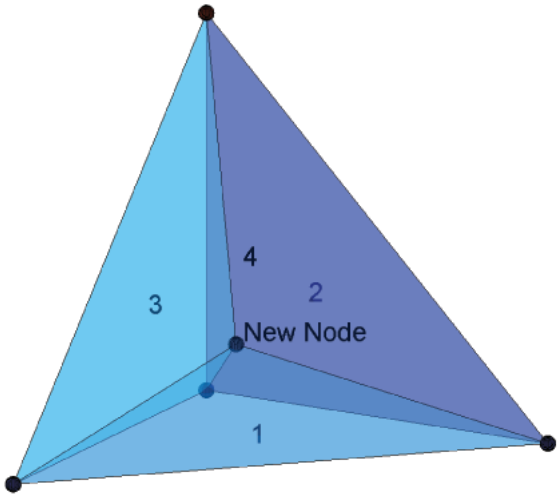

Figure 3.11: Defining a new node and breaking an element into four new smaller elements

3.5 Reconstructing 2D MR images

Now, we would like to discuss how the FEM approximates the continuous deformation throughout each element based on the displacements of the mesh nodes. First, we derive the interpolation (variation) functions for scalar displacement (one dimensional displacement value), and then we extend the theory to the 3D case. In Figure 3.9, a flat-faced tetrahedral element with four nodes labeled as i, j, k, and l is depicted. The values of the field (one dimensional (1D) displacement value in our case) are Φ_i, Φ_j, Φ_k, and Φ_l, and the global positions of the nodes are (x_i, y_i, z_i), (x_j, y_j, z_j), (x_k, y_k, z_k), and (x_l, y_l, z_l) for the nodes i, j, k, and l, respectively. Linear assumption of the interpolation results in the following form of the 1D displacement value of an arbitrary point

$$\phi(x, y, z) = \alpha_1 + \alpha_2 x + \alpha_3 y + \alpha_4 z. \tag{3.19}$$

The nodal conditions causes $\phi(x_i, y_i, z_i) = \Phi_i$, $\phi(x_j, y_j, z_j) = \Phi_j$, $\phi(x_k, y_k, z_k) = \Phi_k$, and $\phi(x_l, y_l, z_l) = \Phi_l$. Therefore, the following system of equations is produced

$$\begin{aligned} \Phi_i &= \alpha_1 + \alpha_2 x_i + \alpha_3 y_i + \alpha_4 z_i, \\ \Phi_j &= \alpha_j + \alpha_2 x_j + \alpha_3 y_j + \alpha_4 z_j, \\ \Phi_k &= \alpha_k + \alpha_2 x_k + \alpha_3 y_k + \alpha_4 z_k, \\ \Phi_l &= \alpha_l + \alpha_2 x_l + \alpha_3 y_l + \alpha_4 z_l. \end{aligned} \tag{3.20}$$

Solving the Eqs. (3.20) gives

$$\begin{aligned} \alpha_1 &= \frac{1}{6V}(a_i\Phi_i + a_j\Phi_j + a_k\Phi_k + a_l\Phi_l), \\ \alpha_2 &= \frac{1}{6V}(b_i\Phi_i + b_j\Phi_j + b_k\Phi_k + b_l\Phi_l), \\ \alpha_3 &= \frac{1}{6V}(c_i\Phi_i + c_j\Phi_j + c_k\Phi_k + c_l\Phi_l), \\ \alpha_4 &= \frac{1}{6V}(d_i\Phi_i + d_j\Phi_j + d_k\Phi_k + d_l\Phi_l), \end{aligned} \tag{3.21}$$

where V is the volume of the tetrahedron given by

$$V = \frac{1}{6}\begin{vmatrix} 1 & x_i & y_i & z_i \\ 1 & x_j & y_j & z_j \\ 1 & x_k & y_k & z_k \\ 1 & x_l & y_l & z_l \end{vmatrix}, \tag{3.22}$$

$$a_i = \begin{vmatrix} x_j & y_j & z_j \\ x_k & y_k & z_k \\ x_l & y_l & z_l \end{vmatrix}, \tag{3.23}$$

$$b_i = \begin{vmatrix} 1 & y_j & z_j \\ 1 & y_k & z_k \\ 1 & y_l & z_l \end{vmatrix}, \tag{3.24}$$

$$c_i = -\begin{vmatrix} x_j & 1 & z_j \\ x_k & 1 & z_k \\ x_l & 1 & z_l \end{vmatrix}, \tag{3.25}$$

and

$$d_i = -\begin{vmatrix} x_j & y_j & 1 \\ x_k & y_k & 1 \\ x_l & y_l & 1 \end{vmatrix}, \tag{3.26}$$

and other constants are defined by cyclic interchange of the subscripts in the order of l, i, j, k. The sign in front of the determinants are to be reversed when a_j, b_j, c_j, d_j and a_l, b_l, c_l, d_l are being generated [26]. Substituting Eq. (3.19) in Eqs. (3.21) results into

$$\begin{aligned} \phi(x,y,z) &= N_i(x,y,z)\Phi_i + N_j(x,y,z)\Phi_j + N_k(x,y,z)\Phi_k + N_l(x,y,z)\Phi_l \\ &= [N(x,y,z)]\vec{\Phi}^{(e)}, \end{aligned} \tag{3.27}$$

where

$$\begin{aligned}
[N(x,y,z)] &= [N_i(x,y,z)N_j(x,y,z)N_k(x,y,z)N_l(x,y,z)] \\
N_i(x,y,z) &= \frac{1}{6V}(a_i + b_i x + c_i y + d_i z) \\
N_j(x,y,z) &= \frac{1}{6V}(a_j + b_j x + c_j y + d_j z) \\
N_k(x,y,z) &= \frac{1}{6V}(a_k + b_k x + c_k y + d_k z) \\
N_l(x,y,z) &= \frac{1}{6V}(a_l + b_l x + c_l y + d_l z)
\end{aligned} \tag{3.28}$$

and

$$\vec{\Phi}^{(e)} = \begin{bmatrix} \Phi_i \\ \Phi_j \\ \Phi_k \\ \Phi_l \end{bmatrix}. \tag{3.29}$$

This is the result of the interpolation function for a scalar (1D) displacement. Extending interpolation function for 3D displacement, which means to have displacement for X, Y and Z directions, we obtain

$$\vec{\phi}(x,y,z) = \begin{bmatrix} u(x,y,z) \\ v(x,y,z) \\ w(x,y,z) \end{bmatrix} = [N(x,y,z)]\vec{\Phi}^{(e)}, \tag{3.30}$$

where

$$[N(x,y,z)] = \begin{bmatrix} N_i(x,y,z) & 0 & 0 & N_j(x,y,z) \\ 0 & N_i(x,y,z) & 0 & 0 \\ 0 & 0 & N_i(x,y,z) & 0 \\ 0 & 0 & N_k(x,y,z) & 0 \\ N_j(x,y,z) & 0 & 0 & N_k(x,y,z) \\ 0 & N_j(x,y,z) & 0 & 0 \\ 0 & N_l(x,y,z) & 0 & 0 \\ 0 & 0 & N_l(x,y,z) & 0 \\ N_k(x,y,z) & 0 & 0 & N_l(x,y,z) \end{bmatrix}, \tag{3.31}$$

$$\vec{\Phi}^{(e)} = \begin{bmatrix} \Phi_{3i-2} \\ \Phi_{3i-1} \\ \Phi_{3i} \\ \Phi_{3j-2} \\ \Phi_{3j-1} \\ \Phi_{3j} \\ \Phi_{3k-2} \\ \Phi_{3k-1} \\ \Phi_{3k} \\ \Phi_{3l-2} \\ \Phi_{3l-1} \\ \Phi_{3l} \end{bmatrix}. \tag{3.32}$$

It should be noted that $u(x, y, z)$, $v(x, y, z)$ and $w(x, y, z)$ are the displacements along X, Y and Z directions, respectively. Also, for each node, we have $u_i = \Phi_{3i-2}$, $v_i = \Phi_{3i-1}$, and $w_i = \Phi_{3i}$. The rest of the displacements are generated by interchanging i with j, k and l.

To reconstruct the 2D deformed MR image, we utilize both the deformed and the un-deformed meshes. Basically, any point on the grid of the MR image will fall inside an element of the deformed mesh. In Figure 3.12(a), a grid point G on Plane A, is assumed to be inside a particular element. Our goal is to find the position of this particular point in the un-deformed mesh. Since the un-deformed and the deformed meshes are available, we have the displacements for each of the four nodes describing a tetrahedron. We are then able to determine the displaced position of every point inside an element (e.g. $\hat{G}$ in Figure 3.12(b)) using the interpolation equations previously introduced. To benefit from the interpolation functions, there are two possible approaches. The first approach is the backward method and it means that $\hat{G}$, the non-displaced position of point G, is determined with this assumption that G is the non-displaced position of point $\hat{G}$. In fact, we replace the two elements with each other. The main advantage of this method is the simplicity of the concept. The only thing that should be considered is to change the sign of the displacement for each node or a negative sign in front of the Eq. (3.32). The second approach or the forward method is explained in what follows.

In the forward method, we assume for every point in the geometry we have

$$\hat{G} = G + \phi(x, y, z). \tag{3.33}$$

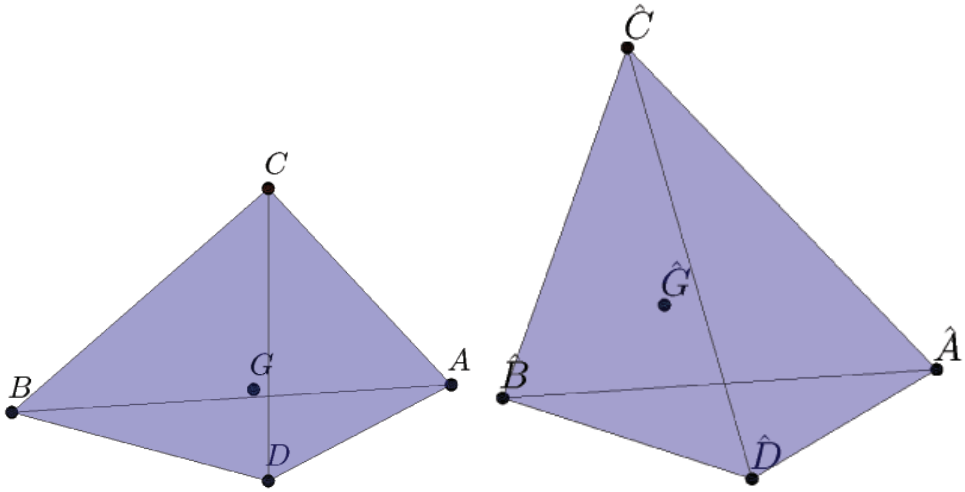

(a) Un-deformed tetrahedron element (b) Deformed tetrahedron element

Figure 3.12: Determining the displacement of an arbitrary point inside an element

According to Eq. (3.30) and Eqs. (3.20), we have the following equations for ϕ

$$\begin{aligned} \phi &= \begin{bmatrix} u \\ v \\ w \end{bmatrix} \\ u &= \alpha_1 + \alpha_2 x + \alpha_3 y + \alpha_4 z \\ v &= \alpha_5 + \alpha_6 x + \alpha_7 y + \alpha_8 z \\ w &= \alpha_9 + \alpha_{10} x + \alpha_{11} y + \alpha_{12} z. \end{aligned} \tag{3.34}$$

Substituting Eqs. (3.34) in Eq. (3.33) gives

$$\begin{bmatrix} \acute{x} \\ \acute{y} \\ \acute{z} \end{bmatrix} = \begin{bmatrix} x \\ y \\ z \end{bmatrix} + \begin{pmatrix} \alpha_1 & \alpha_2 & \alpha_3 & \alpha_4 \\ \alpha_5 & \alpha_6 & \alpha_7 & \alpha_8 \\ \alpha_9 & \alpha_{10} & \alpha_{11} & \alpha_{12} \end{pmatrix} \begin{bmatrix} 1 \\ x \\ y \\ z \end{bmatrix}, \tag{3.35}$$

where $\acute{x}$, $\acute{y}$ and $\acute{z}$ represent $\hat{G}$ or the displaced positions of x, y and z (G), respectively. We should note that α_i's can be obtained with the equations given for the 3D displacement linear interpolation functions, Eqs. (3.35). After some manipulations, we can simply rewrite Eq. (3.35) in the following form:

$$\begin{pmatrix} 1+\alpha_2 & \alpha_3 & \alpha_4 \\ \alpha_6 & 1+\alpha_7 & \alpha_8 \\ \alpha_{10} & \alpha_{11} & 1+\alpha_{12} \end{pmatrix} \begin{bmatrix} x \\ y \\ z \end{bmatrix} = \begin{bmatrix} \acute{x}-\alpha_1 \\ \acute{y}-\alpha_5 \\ \acute{z}-\alpha_9 \end{bmatrix}. \tag{3.36}$$

Our goal was to find G. This is possible by obtaining the inverse of the 3×3 matrix of the Eq. (3.36), and multiplying it by the right hand side of that equation.

The difference between these two methods (forward and backward) is in the speed. In the forward approach, we use the constants of the un-deformed mesh. It is obvious that these constants can be calculated off-line, since the un-deformed mesh is available to us anytime during the deformable registration. On the other hand, the backward approach deals with computing the constants for every deformed mesh. This is especially important in those parts of our algorithm in which we generate different deformed mesh throughout different iterations. Therefore, the algorithm that we used to compute the un-deformed or non-displaced position of a grid point is the

forward method.

Now, the pixel value for this point is found by means of a 3D linear interpolation in the coordinate of the 3D MR data set. This process should be repeated for every grid point to produce the 2D deformed MR image.

3.6 MLS-based Deformations

The Moving Least Squares (MLS) method for image deformation was introduced by Schaefer et al. [28]. The original idea of moving least squares was first proposed by Lancaster and Salkauskas [19]. The main advantages of this method are its smoothness and the minimum amount of local shearing and scaling. To deform an image, a set of control points and their corresponding displaced positions should be selected on the image. For every point v on the image, a least squares problem is solved to find the best affine transformation l_v for that specific point

$$\min \sum_i w_i |l_v(p_i) - q_i|^2, \quad \text{w.r.t. } l_v(x) \text{ as a } 2\times 2 \text{ matrix} \tag{3.37}$$

where p_i and q_i are row vectors representing the initial and the displaced positions of the control points, respectively. Weight coefficients, w_i, are functions of the point v in the form of

$$w_i = \frac{1}{|p_i - v|^{2\alpha}}, \tag{3.38}$$

where $\alpha \geq 1$.

Because the weights w_i in this least squares problem are dependent on the point of evaluation v, we call this a *Moving Least Squares* minimization. Therefore, we obtain a different transformation $l_v(x)$ for each v. We define our deformation function

f to be $f(v) = l_v(v)$. Note that as v approaches p_i, w_i approaches infinity and the function f interpolates; $f(p_i) = q_i$. Moreover, if $q_i = p_i$, then $l_v(x) = x$ for all x and f is the identity transformation $f(v) = v$. Finally, this deformation function f has the property that it is smooth everywhere (except at the control points p_i when $\alpha \leq 1$). Since $l_v(x)$ is an affine transformation, it consists of a linear transformation matrix M and a translation matrix T ($l_v(x) = xM + T$). We can simplify this minimization by removing T. Therefore, by taking the partial derivatives of Eq. (3.37) with respect to free variables in T and setting them to zero a linear system of equations is produced and solving it for T yields $T = q_* - p_*M$, where $p_* = \frac{\sum_i w_i p_i}{\sum_i w_i}$ and $q_* = \frac{\sum_i w_i q_i}{\sum_i w_i}$. With this fact, we can rewrite $l_v(x)$ in terms of linear transformation matrix M

$$l_v(x) = (x - p_*)M + q_*. \tag{3.39}$$

Correspondingly, we are able to turn the first least squares problem into

$$\min \sum_i w_i |\hat{p}_i M - \hat{q}_i|^2, \tag{3.40}$$

where $\hat{p}_i = p_i - p_*$ and $\hat{q}_i = q_i - q_*$. It is clear that this problem is very general and we have many choices for the transformation matrix M. We first derive the closed-form solution to MLS problem by assuming that M is an affine transformation and then similarity transformation. Eventually, we find the solution for M as a rigid transformation, which we are more interested in.

By assuming M as an affine transformation, it has the following form

$$M = \begin{pmatrix} \cos(\alpha) & -\sin(\alpha) \\ \sin(\alpha) & \cos(\alpha) \end{pmatrix} . \begin{pmatrix} 1 & H_x \\ H_y & 1 \end{pmatrix} . \begin{pmatrix} S_x & 0 \\ 0 & S_y \end{pmatrix}, \tag{3.41}$$

where the matrices are called rotation, scaling, and shearing from left to right. Using the classic normal equations solution for Eq. (3.40) (as introduced in [22]), we have

$$f_a(v) = \sum_j A_j \hat{q}_j + q_*, \tag{3.42}$$

where A_j is a single scalar given by

$$A_j = (v - p_*) \left(\sum_i \hat{p}_i^T w_i \hat{p}_i \right)^{-1} \hat{p}_j^T. \tag{3.43}$$

Given a point v, everything in A_j can be simply pre-computed resulting a simple, weighted sum. This deformation can be performed in the order of millisecond on an average Pentium IV machine.

Similarity transformation is a kind of affine transformation that includes translation, rotation and uniform scaling. Hence,

$$M = \begin{pmatrix} \cos(\alpha) & -\sin(\alpha) \\ \sin(\alpha) & \cos(\alpha) \end{pmatrix} . \begin{pmatrix} S & 0 \\ 0 & S \end{pmatrix}. \tag{3.44}$$

To change our deformation method to be restricted to similarity transformation, we limit the matrix M to have the property that $M^T M = \lambda^2 I$ for some scalar λ. M

is a block matrix of the form

$$M = \begin{pmatrix} M_1 & M_2 \end{pmatrix},$$

where M_1 and M_2 are column vectors of length 2. The restriction we have assumed, requires $M_1^T M_1 = M_2^T M_2 = \lambda^2$ and $M_1^T M_2 = 0$. This makes $M_2 = M_1^{\perp}$, where $\perp$ operator means $(x, y) \rightarrow (-y, x)$. With these assumptions about M, the solution to the least squares problem would be

$$f_s(v) = \sum_i \hat{q}_i (\frac{1}{\mu_s} A_i) + q_*, \tag{3.45}$$

where μ_s and A_i depend only on the p_i, v. They can be pre-computed and derived by the following equations

$$\begin{aligned} \mu_s &= \sum_i w_i \hat{p}_i \hat{p}_i^T, \\ A_i &= w_i \begin{pmatrix} \hat{p}_i \\ -\hat{p}_i^{\perp} \end{pmatrix} \begin{pmatrix} v - p_* \\ -(v - p_*)^{\perp} \end{pmatrix}^T. \end{aligned} \tag{3.46}$$

As we expected, similarity MLS deformation preserves angles in the original image better than affine transformation. We observe Figure 3.13(c), which is deformed using similarity transformation, is much better than the result in Figure 3.13(b) using affine transformation. However, there is still one important problem, which is the bigger arm in comparison to the original image. We fix this issue with finding and applying a rigid transformation. For rigid transformation, we use exactly the same equation as for similarity transformation except a modified μ_r. In this case, matrix M will be

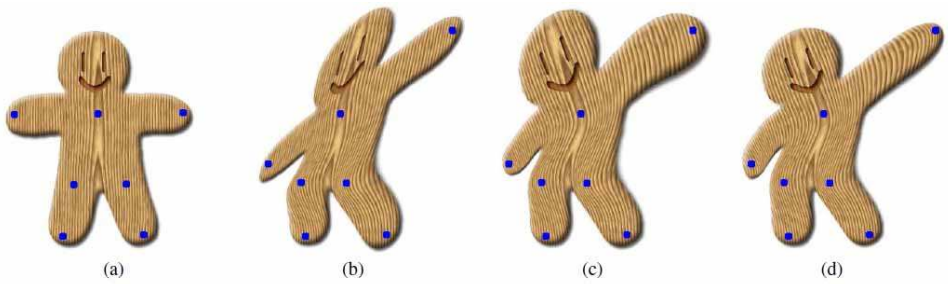

Figure 3.13: Deformation using MLS. Original image with control points shown in blue (a). MLS deformations using affine transformations (b), similarity transformations (c) and rigid transformations (d). Images from [28].

in the following form

$$M = \begin{pmatrix} \cos(\alpha) & -\sin(\alpha) \\ \sin(\alpha) & \cos(\alpha) \end{pmatrix} \tag{3.47}$$

We will not present the mathematics behind this solution and refer the reader to [28] for details. The solution in this case is given by

$$f_r(v) = |v - p_*| \frac{\overrightarrow{f}_r(v)}{|\overrightarrow{f}_r(v)|} + q_*, \tag{3.48}$$

where $\overrightarrow{f}_r(v) = \sum_i \hat{q}_i A_i$ and A_i is defined in Eq. (3.46).

Due to the normalization, this method would be slower than the previous two methods. The result of applying rigid transformation to the doll image can be seen in Figure 3.13(d). It is clear that this is the best deformation among all the methods we have mentioned.

Furthermore, the MLS method can be extended to find the mapping function with respect to another handle like line segment rather than point [28]. In this thesis, another aspect of the presented version of MLS method is extended. In fact, we discuss the 3D extension of 2D MLS method in Section 3.7 as introduce by [34]. 3D

MLS is more useful for our deformable registration problem, since we deform the entire MR volume, and then reconstruct a 2D image from the deformed volume.

3.7 3D MLS-Based Deformations

In the 3D case, solving the minimization problem needs minor modifications. The closed-form solution of Eq. (3.37) for a rigid transformation cannot be derived by the method introduced for the 2D case. For 3D transformation, we use Singular Value Decomposition (SVD) to find a closed-form solution.

If l_v is a rigid transformation then $l_v(x) = Mx + r$, where M is an orthogonal matrix, and r is the translational component. Weighted centroids of p_i's and q_i's are in the following forms [34]

$$p_* = \frac{\sum_i w_i p_i}{\sum_i w_i}, \tag{3.49}$$

$$q_* = \frac{\sum_i w_i q_i}{\sum_i w_i}. \tag{3.50}$$

Note that the translational component of l_v must map p_* to q_* due to the interpolation property of the MLS, which means $r = q_* - p_*$. Therefore, only M should be determined. Let $\alpha_i = w_i^{\frac{1}{2}}$, $\tilde{p}_i = p_i - p_*$, $\tilde{q}_i = q_i - q_*$, $P = \alpha_i(\tilde{p}_1 \cdots \tilde{p}_N)$, $Q = \alpha_i(\tilde{q}_1 \cdots \tilde{q}_N)$ (P and Q are 3 by N matrices). Then

$$\begin{aligned} E &= \sum_i w_i |M\tilde{p}_i - \tilde{q}_i|^2 = \sum_i |M\alpha_i\tilde{p}_i - \alpha_i\tilde{q}_i|^2 \\ &= \|MP - Q\|_F^2 = tr((MP-Q)^t(MP-Q)) \\ &= tr(P^tP) + tr(Q^tQ) - 2tr(Q^tMP), \end{aligned} \tag{3.51}$$

where $\|.\|_F$ denotes the Frobenius norm. Maximizing $\zeta = tr(Q^tMP) = tr(MPQ^t)$ causes E to be minimized, since P and Q are constant. According to SVD, $PQ^t = U\Lambda V^t$ such that $\Lambda = diag(\lambda_1, \lambda_2, \lambda_3)$ is diagonal with non-negative entries, and U, V are orthogonal. Hence

$$\zeta = tr(MPQ^t) = tr(MU\Lambda V^t) = tr(U^tM^tV\Lambda). \tag{3.52}$$

Let $N = U^tM^tV$, then N is orthogonal due to the fact that U, M, and V are all orthogonal. Consequently, $|N_{i,j}| \leq 1$, and

$$\zeta = tr(N\Lambda) = \sum_{i=1}^{3} N_{i,i}\lambda_i \leq \sum_{i=1}^{3} \lambda_i. \tag{3.53}$$

Thus, ζ is maximized, when $N = 1 \Leftrightarrow M = VU^t$ [34].

To summarize, by calculating p_* and q_* and performing SVD on PQ^t, finally we can let

$$l_v(x) = VU^t(x - p_*) + q_*. \tag{3.54}$$

In the MLS-based method, we replace initial control points with the features selected on the 2D MR image and also the displaced control points with the features selected on the ultrasound image. Our goal is to find a rigid transformation based on Eq. (3.54) for every point in the MR volume. The entire process of our algorithm is depicted in Figure 3.14. Due to the high computational complexity of this approach, we calculate this transformation for every point on a coarse low resolution 3D grid, which we build based on our 3D volume. By decreasing the number of points with computed deformation, we can interpolate the displacement in all three directions (X, Y, and Z) for any point inside the volume. Using a linear interpolation with known

displacements for a set of regularly placed points (points on 3D low resolution grid), we are able to interpolate the displacements for any point inside the MR volume. Therefore, to reconstruct the 2D MR image, we first use the approach explained in Section 3.1 to find the grid points on the plane of the 2D MR image. Then, for each point using the mentioned displacement interpolation, the new positions of these grid points are obtained. Next, the pixel intensities are interpolated by means of a 3D linear interpolation. Putting all these pixel intensities together in a 2D matrix, provides us with a 2D deformed MR image reconstructed on the desired plane.

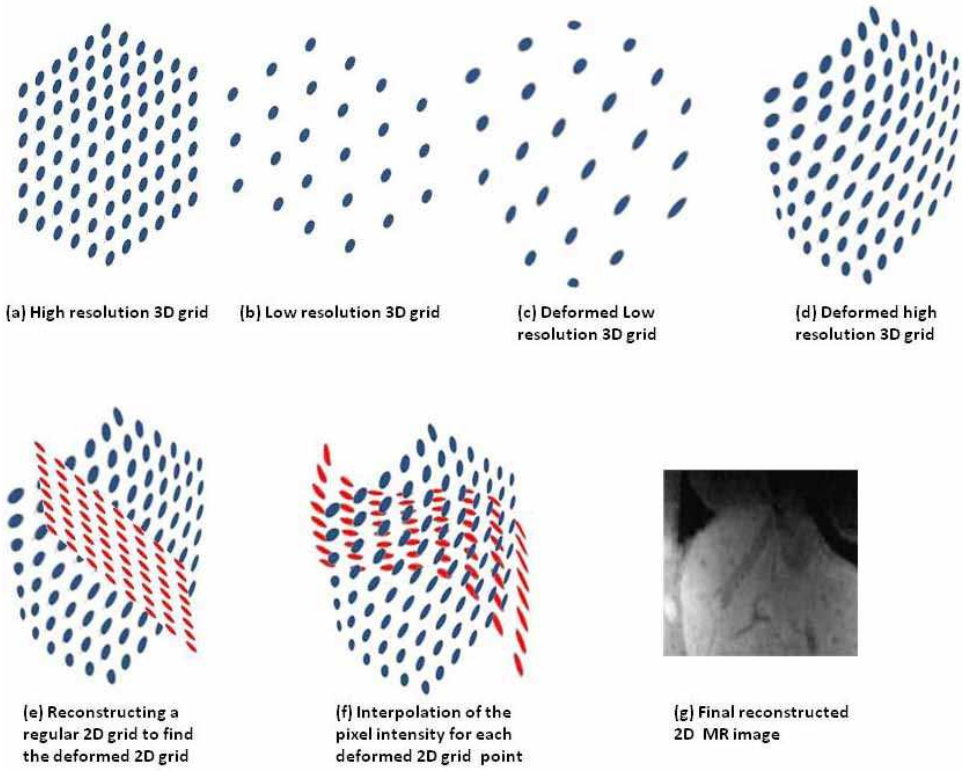

Figure 3.14: Obtaining a deformed 2D MR image based on the deformed MR volume. The process starts with the conversion of a high resolution 3D grid (a) into a low resolution one (b). By applying the solution of Eq. (3.54) to each grid point in (b) deformed grid (c) is built. Using 3D interpolation in all three directions a deformed high resolution grid (d) is constructed. The same technique is used to reconstruct a deformed 2D grid (f) from a regular 2D grid (e). Finally, by the interpolation of the intensity the deformed 2D MR image is produced (g).

Chapter 4

Experimental Results

In this Chapter, we provide the reader with the experimental results of our methods. Also, the existing trade-offs between speed and accuracy are being addressed. In Section 4.1, the results of the initial and the deformable registration for the presented methods are evaluated. In Section 4.2, we discuss the speed issues and conclude our work by explaining the final results. Throughout this chapter, we only use one set of data to test our algorithms which seems rather insufficient. It should be noted that collecting the data for this thesis was divided into two parts. The first part was the MR liver imaging, which was not available for us anytime we would like to have access. Therefore, we ended up having only one MR data set of a volunteer within the two years of working on the project. The second part of the data collecting was to acquire the US images of the same volunteer. Due to the lack of an expert operator to obtain the US images with the clinical standards and having only one volunteer, the same person who underwent the MR imaging for a US liver imaging, we decided to let the volunteer acquire the US images himself. The US images are not probably the best we could have, but they seem to satisfy our needs to run the registration

process.

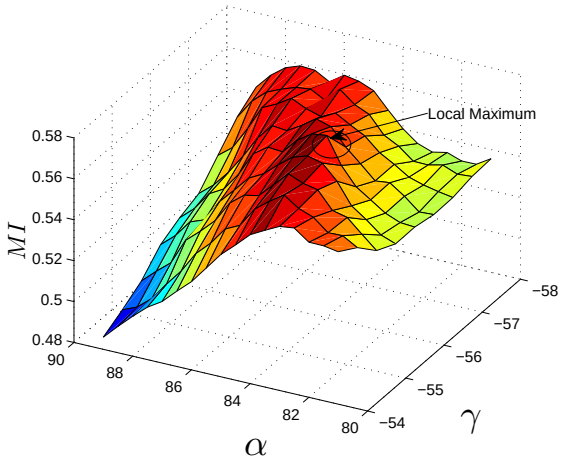

Figure 4.1: Local maximum of the mutual information between I_{US} and I_{MR}. As introduced in 3.1, α and γ are two rotational parameters in degree, while $\beta = 0$, $T_x = 156.3$, $T_y = 53.6$, and $T_z = 224$.

4.1 Initial and Deformable Registration Results

A set of inhale breath-hold MR images was acquired from a healthy liver of a volunteer using a 3T GE MEDICAL SYSTEMS scanner with a body coil. The images were 3-D T1-weighted with the voxel size of 0.59 mm×0.59 mm×4.00 mm. A set of 2D US images were obtained using a SIEMENS SONOLINE G60S and C6-3 probe. The pixel spacing of the US scan was 0.41 mm×0.41 mm. Corresponding 2D MR image, I_{MR}, of the US image, I_{US} as explained in 3, is found by the initial rigid registration. I_{US} and I_{MR} are illustrated in Figures 4.4(a) and 4.4(b), respectively. Figure 4.1 shows the local maximum of the mutual information as defined in Eq. (2.9) as the similarity measure to find the best local MR image match of the US image. This

N	MLS	FEM
4	12.8	9.3
5	12.2	8.7
6	11.5	8.2
10	8.9	7.2

Table 4.1: RMS TRE (in millimeter) for different methods of this thesis with various N (N is the number of control points used to run the methods).

figure illustrates a local maximum of our similarity measure with regard to two of the parameters. This local search is done for all the six rigid parameters, but because of the limitation in representing more than three dimensions, we choose only two of the parameters along with the amount of mutual information.

Figures 4.4(c) and 4.4(a) present the results of the FEM-based and MLS-based methods on I_{MR}. To evaluate the 3D registration accuracy qualitatively, we arbitrarily choose another 2D US image on Plane C in Figure 3.2, called test plane, and find the corresponding 2D MR image. Deformable registration using FEM-method and MLS-method is performed, and the two resulting deformed MR images are displayed in Figure 4.3. Also, the results of our methods for the reference planes (Plane A and B in Figure 3.2) are showed in Figures 4.4 and 4.5.

Quantitative evaluation of our methods is carried out by calculating RMS TRE between the deformed MR test image and the US test image. Two sets of points on the two images are chosen (Q_{MR} and Q_{US}). These points display the corresponding structures on both images. A sample of such points can be illustrated in Figure 3.10. The TRE for a pair of points (Q^i_{MR} and Q^i_{US}) is defined as

$$TRE = Q^i_{MR} - Q^i_{US} \tag{4.1}$$

The RMS TRE is then calculated for all of the points, and consequently we can have a quantitative evaluation of our registration. In Table 4.1, we computed the RMS TRE for various numbers of control points for both methods we introduced. It can be seen that FEM-based method with $N = 10$ results in the best performance for the registration. We examined higher values of N, but no significant improvement in terms of RMS TRE was observed. MLS-based method performs as an acceptable registration with RMS TRE of 8.9 mm with $N = 10$. However, due to the fact that FEM-based method contains some information (very rough approximation) on the real organ deformation, it seems reasonable that it outperforms MLS-based method. Basically, MLS-based method is purely deduced by mathematical models. It should be noted that the cost of using FEM-based method instead of MLS-based method is the higher computational complexity.

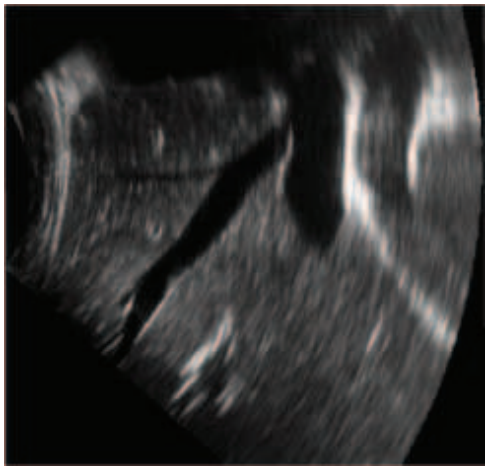

(a) Test US image

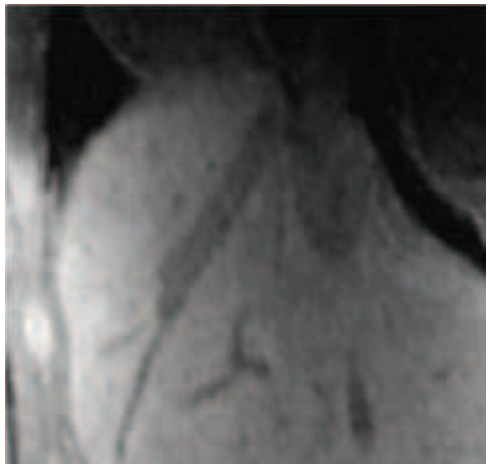

(b) Correctly deformed MR image, MI=0.4989

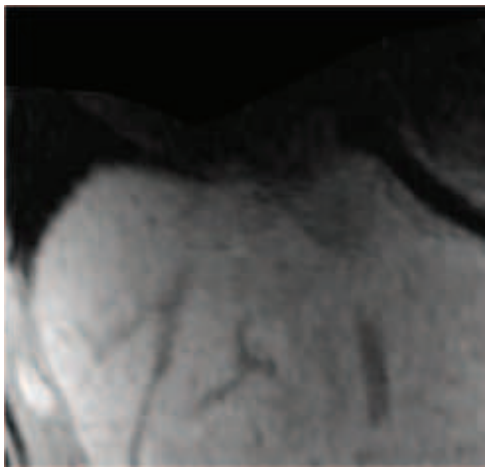

(c) False deformed MR image, MI=0.6130

Figure 4.2: False registration by mutual information. The deformed MR images are produced with FEM-based method with N=10. Mutual information for each MR image is calculated between I_{US} and I_{MR}.

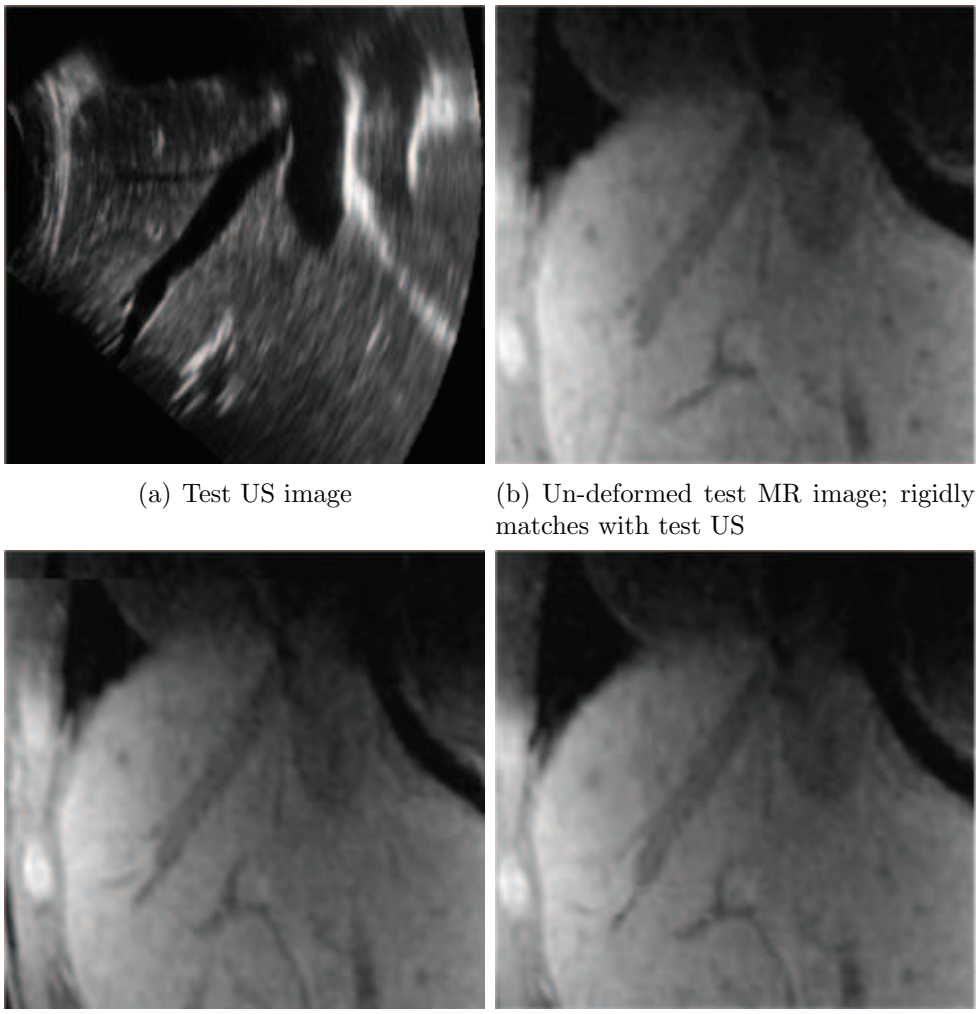

(a) Test US image

(b) Un-deformed test MR image; rigidly matches with test US

(c) Deformed test MR image using MLS-based method

(d) Deformed test MR image using FEM-based method

Figure 4.3: Test US and its rigid and non-rigid MR image matches using FEM and MLS (Geometrical Plane C in Figure 3.2).

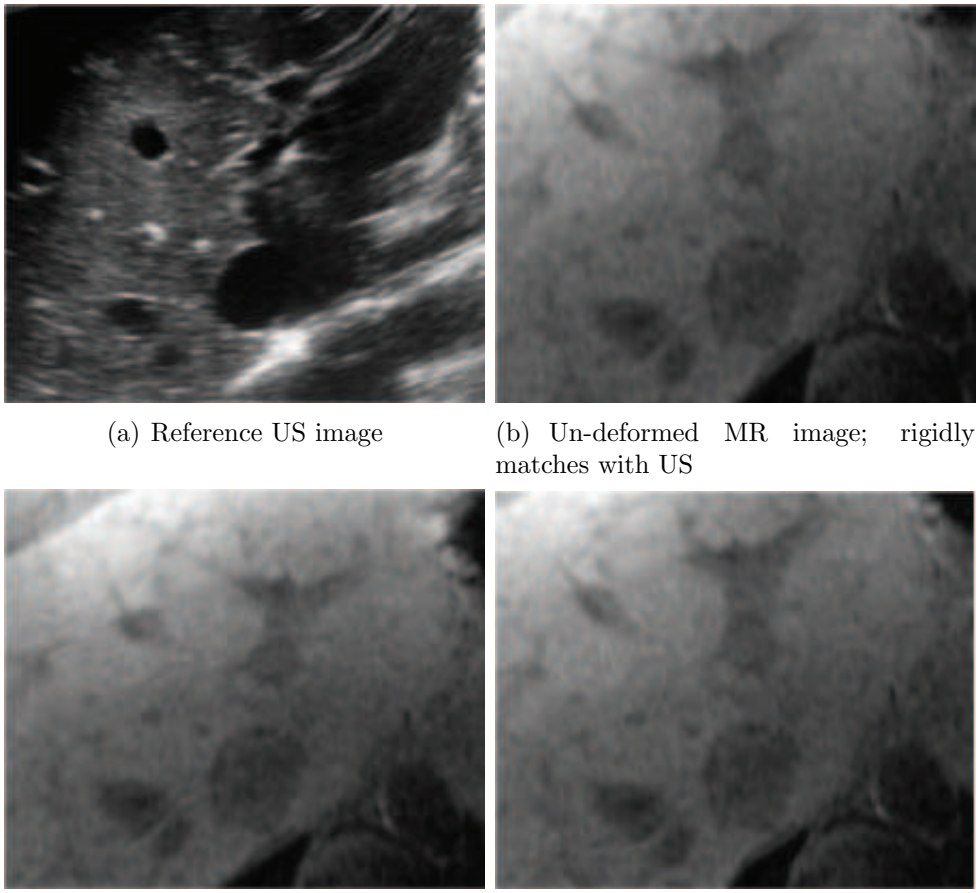

(a) Reference US image

(b) Un-deformed MR image; rigidly matches with US

(c) Deformed MR image using MLS-based method

(d) Deformed MR image using FEM-based method

Figure 4.4: Reference US and its rigid and non-rigid MR image matches using FEM and MLS (Geometrical Plane A in Figure 3.2).

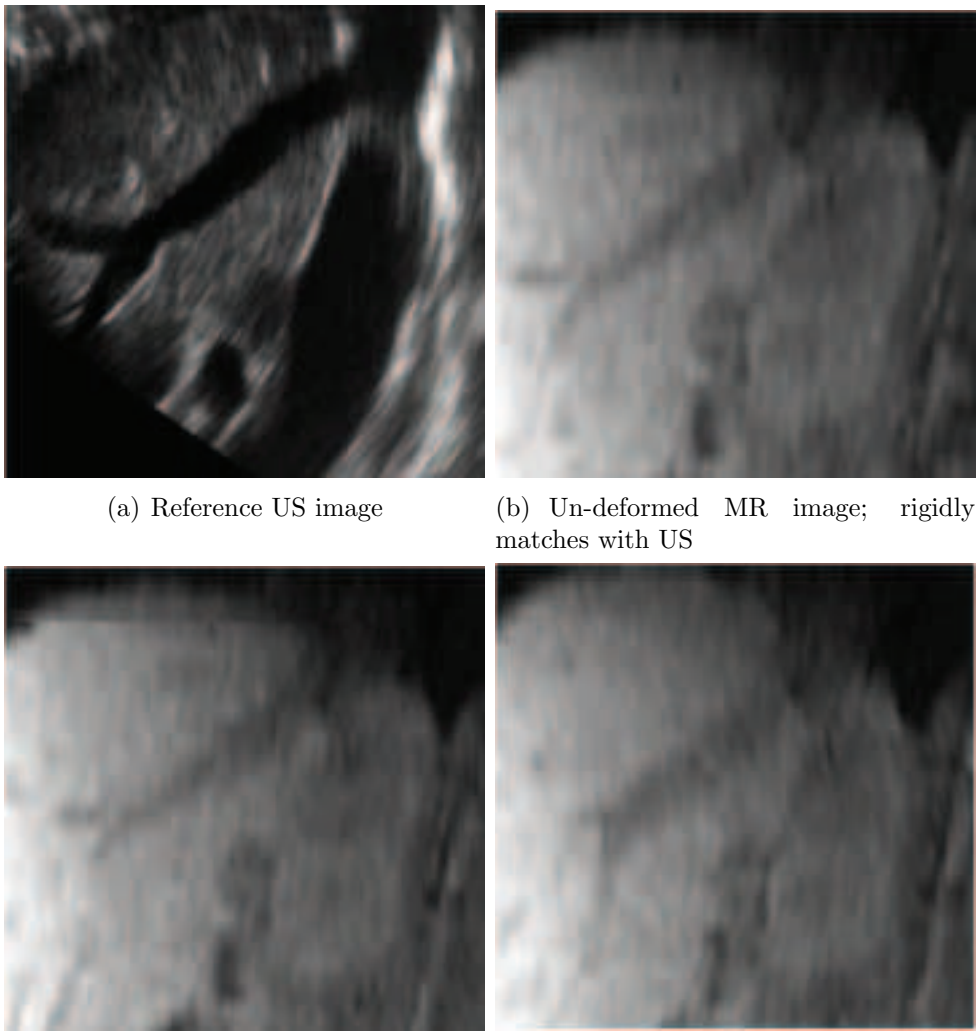

(a) Reference US image

(b) Un-deformed MR image; rigidly matches with US

(c) Deformed MR image using MLS-based method

(d) Deformed MR image using FEM-based method

Figure 4.5: Reference US and its rigid and non-rigid MR image matches using FEM and MLS (Geometrical Plane B in Figure 3.2).

It is worth mentioning that mutual information as a quantitative evaluation has been tested. False registration results which are corresponding to higher amount of mutual information as similarity criterion between I_{US} and I_{MR} on the test plane (plane C in Figure 3.2), indicates that mutual information cannot be used as a reliable evaluation criteria. As an evidence, Figure 4.2 represents I_{US} on the test plane along with the two different deformed MR images. Image (b) is the correctly deformed I_{MR} match of I_{US} with lower amount of mutual information (0.4989) and a RMS TRE of 7.2mm, while image (c) is the deformed I_{MR} with higher amount of mutual information (0.6130). Therefore, mutual information cannot be used as a useful measure of accuracy. It should be noted that the RMS TRE for the false I_{MR} cannot be computed, since the anatomy structures of I_{US} are not completely present on this image. The inherent problem with mutual information is that its value can be significantly dependent to the background noise [12]. US and MR images of the liver have a large number of pixel intensities mostly classified as background noise or irrelevant anatomy structures. Hence, the mutual information as function of registration parameters can possibly have many local peaks due to the alignment of the background noise. Normally, alignment of the important anatomy structures that are used as the landmarks in our algorithms has a very small effect on the value of the mutual information. Therefore, mutual information potentially can results in false registrations.

4.2 Computational Speed and Solutions

M	T	RMS TRE	i	$R^T \cdot R$
23	0.31	10.5	71	3.1818e+003
88	0.58	10.2	125	2.6540e+005
172	1.43	9.1	43	2.2690e+009
587	14.27	9.0	171	2.2973e+003

Table 4.2: Various running time, T, for different numbers of the nodes, M, of the mesh with their corresponding registration accuracy results, RMS TRE, in the FEM-based method. The number of iterations in the CG is denoted by i. The measure of error is $R^T \cdot R$. The vector of residual is calculated as $R = f - K.U$, where f is the force vector, K is the global stiffness matrix, and U is the global nodal displacement vector in FE analysis. In fact, $R^T \cdot R$ should be made small as the error. The CG starting point is set as $U^{i=1} = f$. CG algorithm stops whenever i reaches 900 or $R^T \cdot R$ decreases by the order of 10^{14}. Note that the number of control points used in every row is 4 (N=4).

No. of nodes	Duration (in second)	RMS TRE (in millimeter)
180	0.08	10.8
567	0.23	10.5
1690	0.70	10.2
13520	6.55	10.1

Table 4.3: Various running time for different numbers of the points on the 3D grid with their corresponding registration accuracy results in the MLS-based method. Note that the number of control points used in every row of the table is 4 (N=4).

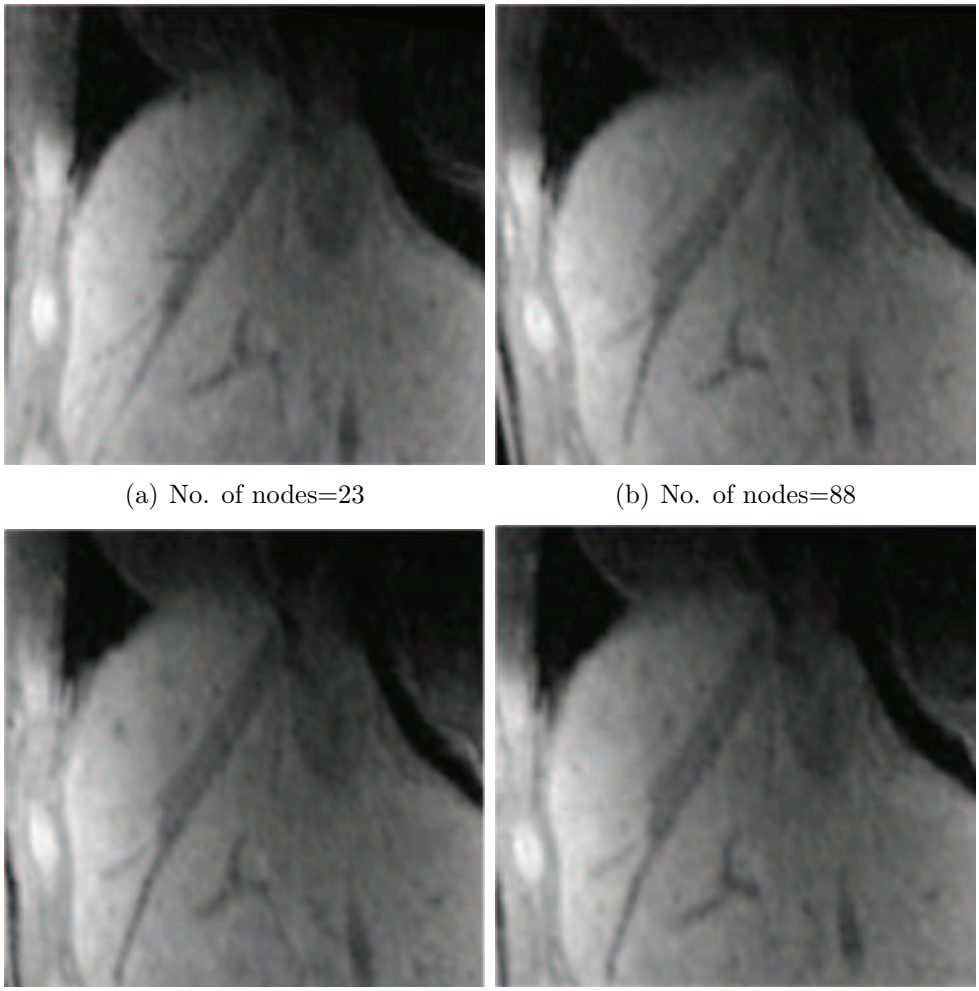

(a) No. of nodes=23 (b) No. of nodes=88

(c) No. of nodes=172 (d) No. of nodes=587

Figure 4.6: Different numbers of the nodes of the mesh with their corresponding registration accuracy results in the FEM-based method. Note that the number of control points used is 4. (The deformed MR image is on the geometrical Plane A in Figure 3.2).

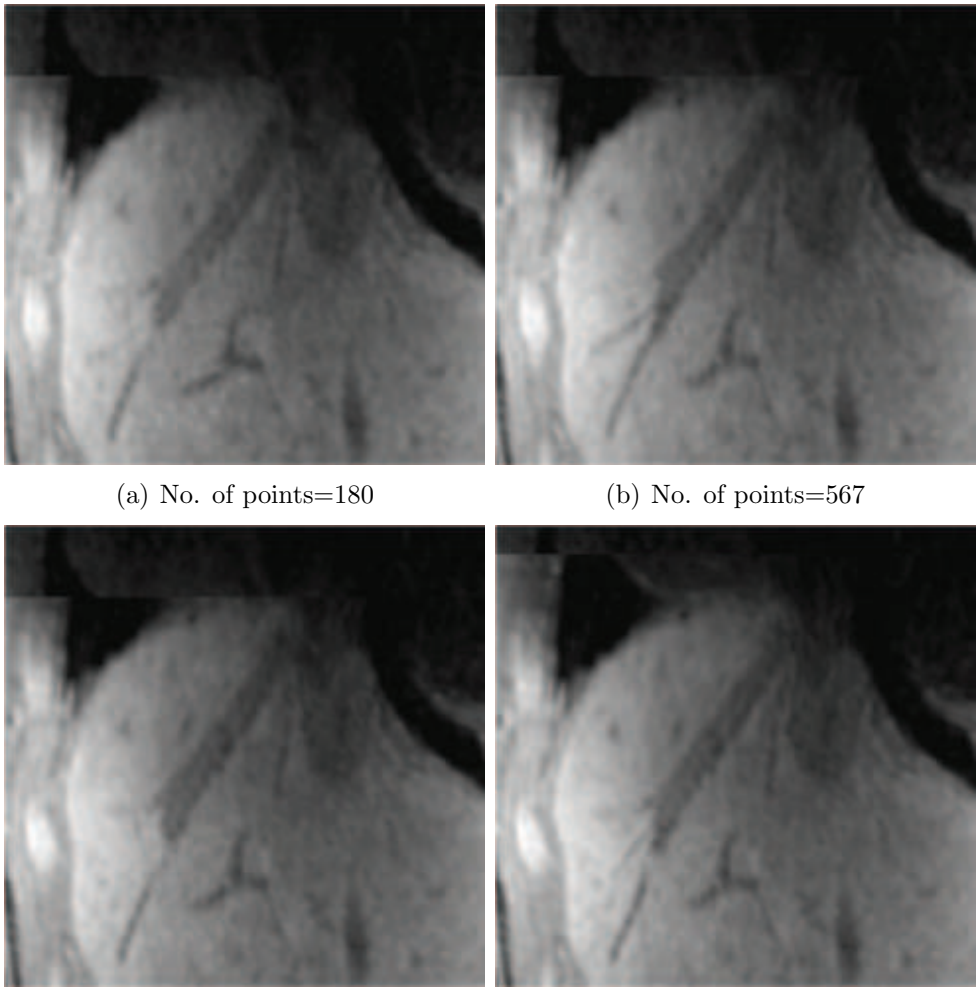

(a) No. of points=180 (b) No. of points=567

(c) No. of points=1690 (d) No. of points=13520

Figure 4.7: Different numbers of the points on the 3D grid with their corresponding registration accuracy results in the MLS-based method. Note that the number of control points used is 4. (The deformed MR image is on the geometrical Plane A in Figure 3.2).

In this section, we discuss the results of the proposed deformable registration algorithm with different grid resolutions. Technically, most of the computational load of the algorithm is related to calculating the deformation for the 3D grid, which we use to obtain the final result for the entire MR volume. In FEM-based method, the resolution of the 3D grid could be the number of the nodes of the organ mesh. The number of the points on the regular 3D grid, that we build to obtain the deformation, determines the resolution of the 3D grid in the MLS-based method. The other important part of the complexity arises from the resolution of the 2D grid. This grid is used to interpolate pixels' intensities to reconstruct a 2D image as the final output of the nonrigid registration. But, because of the different conditions and algorithms used to do this task in the two introduced methods (MLS and FEM), we cannot have an accurate comparison. Therefore, in the following study, we only consider the resolution of the 3D grid, which is the most effective part on the speed of the algorithms.

We test the algorithms on a Pentium IV with a Dual Core 1.66GHz CPU and 2 Gigabytes RAM. For the implementation of the FEM-based and MLS-based methods, we use MATLAB R2007b. Implementation of 3D MLS algorithm includes matrix multiplications and using the SVD function of MATLAB. A MATLAB implementation of the Conjugate Gradient (CG) algorithm is used to solve the linear system of equations of Eq. (3.16). The measure of error is provided by $R^T \cdot R$. This vector of residual is calculated as $R = f - K.U$, where f is the force vector, K is the global stiffness matrix, and U is the global nodal displacement vector in FE analysis. In fact, $R^T \cdot R$ as the error, should be made small. The CG starting point is set as $U^{i=1} = f$. CG algorithm stops whenever i reaches 900 or $R^T \cdot R$ decreases by the

order of 10^{14}. It should be noted that the inputs of the two algorithms are assumed to be prepared and the computation time of this preparation is not calculated in the running time of the algorithms. Also, except for the internal iterations of the SVD function of MATLAB, the MLS-based code is single-iteration only.

Table 4.3, represents the time it takes to compute the deformations for all the points for various grid resolutions. In FEM-based method, this would be the duration of the computing the nodes' displacements. To have a better perspective of the trade-offs here, using both methods, FEM and MLS, the final registered 2D images on Plane A in Figure 3.2 for the selected grid resolutions are displayed in Figures 4.6 and 4.7. Obviously, MLS-based method outperforms FEM-based in terms of speed. For almost the same number of grid points (in average $\sim$ 570 number of points/nodes for both methods), the results of the two methods are given in Figures 4.6(d) and 4.7(b). Comparing with the US image of the same plane, FEM-based method produces RMS TRE of 9.0 mm, while MLS-based method results in RMS TRE of 10.8 mm. Therefore, we can conclude that FEM outperforms MLS. Ultimately, it can be concluded that with a moderate resolution , e.g. 172 for FEM, we can gain a faster speed, while keeping the quality and the accuracy of the registration at an acceptable level.

Chapter 5

Conclusions and Future Work

Deformable multi-modality image registration is a challenging problem due to various types of possible deformations and high chance of false registration. In particular, 3D registration of MR and US is a very difficult task because of the fundamental differences in the nature of the two modalities and the noisy nature of the US images. In this thesis, we initially find a 2D MR match of our acquired 2D US image by means of a tracking system. In the next step, this image is further optimized by a local search of six rigid parameters to maximize the mutual information as a similarity measure between the two images. The main goal of this thesis is to detect the differences, which are caused by deformations between these two images, and apply them to the entire MR volume. This process is accomplished by employing two specialized techniques introduced in Chapter 3: FEM-based and MLS-based methods. FEM-based method benefits from more realistic results due to the fact that it is based on the continuum mechanics, while MLS-based method is purely deduced from mathematical functions, approximation, and interpolation theory. Although, our FE modeling is not completely governed by real parameters of the organ (liver) and we use a linear

elastic model and also unknown boundary conditions, but the preliminary results we obtain by this method illustrates a better accuracy than MLS-based method. Our implementation of the MLS-based method could be executed at least 20 times faster than that of the FEM-based method. Therefore, in applications, where the accuracy is critical, FEM-based method should be used. The MLS-based method is more suitable of the applications demanding higher speed or a parallel implementation of the FEM-based method can solve the computation speed problem.

According to the preliminary results presented in this thesis, there are still numerous potentials for further research including:

- Automatic selection of the control points to have a fully automatic deformable registration algorithm
- Extending the deformable registration algorithm by proposing a cost function which can generate a global optimum in a correct match between the deformed MR image and the US image
- Parallel implementation of the algorithms on FPGA or GPUs to achieve a real-time response
- Increasing the number of reference US images, and using the correlation between them to increase the accuracy of the results
- Building a high quality FE mesh by including the neighboring organs (referred to as *multi-organ mesh*), and increasing the number of nodes
- Obtaining the boundary conditions of the multi-organ mesh to produce more realistic results

- Extension of the current criteria to assess the registration results with a more sophisticated and accurate measurement

Appendix A

Mutual Information

Hill et al. [13] proposed a 2D plot showing the combination of gray values in each of the two images for all corresponding points. This *feature space* is referred to as a joint histogram. The two images should essentially in the same size. The joint histogram is constructed by counting the number of times a combination of gray values occurs. For each pair of corresponding points, (x, y), with x a point on image A and y a point on image B, the entry $(I_A(x), I_B(y))$ in the feature space is increased (I is a function, which maps the position to the intensity in an image). This means that joint histogram is a $m \times n$ matrix, where m and n are the number of available pixel intensities in image A and B, respectively. In Figure A.1(c), we display the joint histogram between image A and B. To represent a better illustration of the joint histogram, we normalize the entries of the join histogram between 0 and 1.

According to the Shannon's definition of join entropy [29], and by dividing each

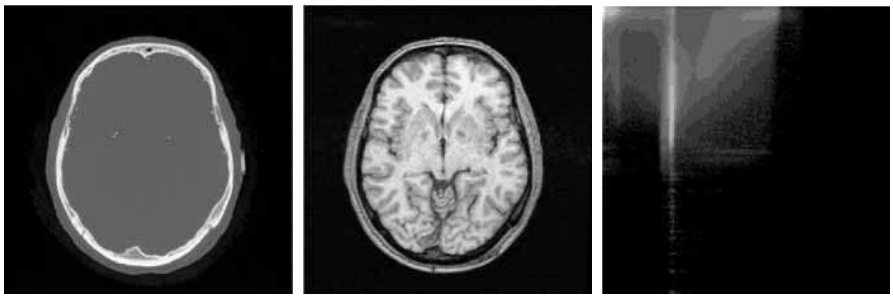

(a) Image A (b) Image B (c) Joint histogram

Figure A.1: Joint histogram of a CT image (A) and a MR image (B). Images from [25]

entry of the joint histogram by the total number of entries, we can write

$$-\sum_{i,j} p(i,j) \log p(i,j),$$

where $p(i,j)$ is the probability of each entry of the joint histogram.

Entropy of an image is computed by dividing the number of occurrence of each pixel intensity by the total number of pixels to find a probability for each pixel intensity. The next step is to calculate the following summation

$$-\sum_{i} p(i) \log p(i).$$

Finally, mutual information is calculated based on Eq. (2.9).

Appendix B

Phantom Study

In this section, we briefly explain how to make a phantom from Poly Vinyle Alcohol (PVA) cryogel based on the method introduced in [8]. A sealed container of aqueous solution of 15.0% by weight PVA was heated in boiling water for an hour. Depending on the concentration of the solution, different hardness of the produced gel can be achieved. It is worth noting that hardness also depends on the number of freeze-thaw cycles. The solution is poured into the final container (or mold) and freezed for twelve hours at $-20\,^{\circ}$C. Then, the container is thawed by raising the air temperature by $10\,^{\circ}$/min to $25\,^{\circ}$C and held at that temperature for twelve hours. This process is called a freeze-thaw cycle. We can continue this cycle to have a harder gel. For the purpose of this thesis, we poured two other layers of PVA solution with a number of arbitrarily placed stones on the top of each layer as the features of the phantom. Therefore, the bottom layer is the hardest and the top layer is the softest layer of the phantom. This multi-modality deformable phantom can be scanned by the US probe from the top layer, since it is inside the container box. A T1 weighted 2D MR image of the phantom is displayed in Figure B.2. The black features are the stones that we

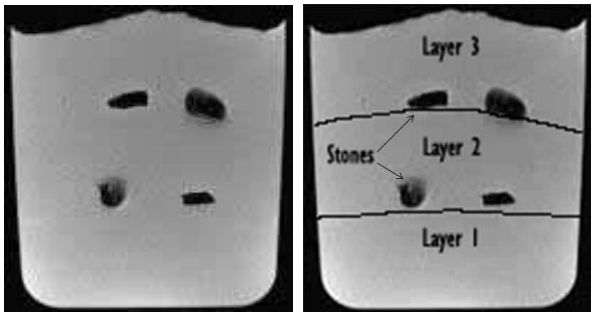

(a) T1 weighted 2D MR image (b) Layers and the stones

Figure B.2: A T1 weighted 2D MR image of the PVA phantom

placed into the solution before the freeze-thaw cycle of the next layer.

Bibliography

[1] M. Alexa, D. Cohen-Or, and D. Levin, *As-rigid-as-possible shape interpolation*, in SIGGRAPH '00: Proceedings of the 27th annual conference on Computer graphics and interactive techniques, New York, NY, USA, 2000, ACM Press/Addison-Wesley Publishing Co., pp. 157–164.

[2] B. Best, *Cancer death – causes & prevention.* `http://www.benbest.com/health/cancer.html`.

[3] J. M. Blackall, G. P. Penney, A. P. King, and D. J. Hawkes, *Alignment of sparse freehand 3-d ultrasound with preoperative images of the liver using models of respiratory motion and deformation*, IEEE Trans. on Medical Imaging, 24 (2005), pp. 1405–1416.

[4] F. L. Bookstein, *Principal warps: Thin-plate splines and the decomposition of deformations*, IEEE Trans. Pattern Anal. Mach. Intell., 11 (Jun. 1989), pp. 567–585.

[5] C. Broit, *Optimal Registration of Deformed Images*, Ph.D. dissertation, Dept. Comput. Inf. Sc., Univ. Pennsylvania, Philadelphia, 1981.

[6] P. C. Chou and N. J. Pagano, *Elasticity: Tensor, Dyadic, and Engineering Approaches*, New York: Dover, 1992.

[7] G. E. Christensen, R. D. Rabbitt, and M. I. Miller, *Deformable templates using large deformation kinematics*, IEEE Trans. Image Process., 5 (Oct. 1996), pp. 1435–1447.

[8] K. C. Chu and B. K. Rutt, *Polyvinyl alcohol cryogel: An ideal phantom material for mr studies of arterial flow and elasticity*, Magn. Reson. Med, 37 (1997), pp. 314–319.

[9] M. D. Craene, A. du Bois dAische, B. Macq, F. Kipfmueller, N. Weisenfeld, S. Haker, and S. Warfield, *Multimodal nonrigid registration using a stochastic gradient approximation*, ISBI, (2004), pp. 1459–1462 Vol. 2.

[10] C. Davatzikos and R. N. Bryan, *Using a deformable surface model to obtain a shape representation of the cortex*, IEEE Trans. Med. Imag., 15 (Dec. 1996],), pp. 785–795.

[11] T. Gaens, F. Maes, D. Vandermeulen, and P. Suetens, *Non-rigid multimodal image registration using mutual information*, in MICCAI '98: Proceedings of the First International Conference on Medical Image Computing and Computer-Assisted Intervention, London, UK, 1998, Springer-Verlag, pp. 1099–1106.

[12] E. Haber and J. Modersitzki, *Intensity gradient based registration and fusion of multi-modal images*, in Methods of Information in Medicine, Schattauer Verlag, 2006, pp. 726–733.

[13] D. L. G. Hill, D. J. Hawkes, N. A. Harrison, and C. F. Ruff, *A strategy for automated multimodality image registration incorporating anatomical knowledge and imager characteristics*, Lecture Notes in Computer Science., 678 (1993), pp. 182–196.

[14] M. Holden, *A review of geometric transformations for nonrigid body registration*, IEEE Trans. on Med. Imag., 27 (Jan. 2008), pp. 111–128.

[15] X. Huang, N. A. Hill, J. Ren, G. Guiraudon, D. Boughner, and T. M. Peters, *Dynamic 3-d ultrasound and mr image registration of the beating heart*, Med. Image Comput. Computer-Assisted InterventionMICCAI, 3750 (2005), p. 171.

[16] J. D. Humphery, *Continuum biomechanics of soft biological tissues*, Proc. R. Stat. Soc., 459 (2003), pp. 3–46.

[17] T. Igarashi, T. Moscovich, and J. F. Hughes, *As-rigid-as-possible shape manipulation*, ACM Trans. Graph., 24 (2005), pp. 1134–1141.

[18] M. R. Kaus and K. K. Brock, *Deformable image registration for radiation therapy planning: algorithms and applications*, World Scientific, 2007, pp. 1–28.

[19] P. Lancaster and K. Salkauskas, *Surfaces generated by moving least squares methods*, Math. Comput., 37 (1981), pp. 141–158.

[20] T. Lange, S. Eulenstein, M. Hnerbein, and P. M. Schlag, *Vessel-based non-rigid registration ofmr/ct and 3d ultrasound for navigation in liver surgery*, Computer Aided Surgery, 8.

[21] T. Lange, N. Papenberg, S. Heldmann, J. Modersitzki, B. Fischer, and P. M. Schlag, *3d ultrasound-ct registration of the liver using combined landmark-intensity information*, Int'l Conf. on Computer Assisted Radiology and Surgery, (2008).

[22] C. F. V. Loan and G. H. Golub, *Matrix Computations*, John Hopkins University Press, 1996.

[23] R. Mafi, *Hardware-based parallel computing for real-time simulation of soft-object deformation*, M.A.Sc. Thesis, McMaster University, (2008).

[24] R. Mafi, S. Sirouspoury, B. Mahdavikhah, B. Moody, A. K. Kaveh Elizeh, and N. Nicolici, *A parallel computing platform for real-time haptic interaction with deformable bodies*, IEEE TRANSACTIONS ON HAPTICS, (2008, in press).

[25] J. Pluim, J. Maintz, and M. Viergever, *Mutual-information-based registration of medical images: a survey*, Medical Imaging, IEEE Transactions on, 22 (2003), pp. 986–1004.

[26] S. S. Rao, *The Finite Element Method in Engineering*, Elsevier Science & Technology Books, 2004.

[27] D. Rueckert, L. I. Sonoda, C. Hayes, D. L. G. Hill, M. O. Leach, and D. J. Hawkes, *Nonrigid registration using free-form deformations: Application to breast mr images*, IEEE Trans. Med. Imag., 18 (Aug. 1999), pp. 712–721.

[28] S. Schaefer, T. Mcphail, and J. Warren, *Image deformation using moving least squares*, In SIGGRAPH 06: ACM SIGGRAPH 2006 Papers, (2006), pp. 533–540.

[29] C. E. Shannon, *A mathematical theory of communication*, Bell Syst. Tech. J., 27 (1948), pp. 379–423.

[30] S. Sirouspour, *Robotic and telerobotic control systems-lecture notes, winter 2009*. Available from Department of Electrical and Compuetr Engineering of McMaster University.

[31] J. P. Thirion, *Image matching as a diffusion process: An analogy with maxwell's demons*, Med. Image Anal., 2 (Sep. 1998), pp. 243–260.

[32] J. Weese, P. Rche, T. Netsch, T. Blaffert, and M. Quist, *Gray-value based registration of ct and mr images by maximization of local correlation*, Medical Imaging Computing and Computer-Assisted Intervention MICCAI, (1999), pp. 656–663.

[33] W. Wein, S. Brunke, A. Khamene, M. Callstrom, and N. Navab, *Automatic ct-ultrasound registration for diagnostic imaging and image-guided intervention*, Medical Image Analysis, 12 (2008), pp. 577–585.

[34] Y. Zhu and S. J. Gortler, *3d deformation using moving least squares*, 2007.

[35] B. Zitová and J. Flusser, *Image registration methods: a survey*, Image and Vision Computing, 21 (2003), pp. 977–1000.